027723-4-T

# ELECTROMAGNETIC CHARACTERIZATION OF CONFORMAL ANTENNAS

J. L. Volakis, L. C. Kempel, A. Alexanian, J. M. Jin, C. L. Yu and A. C. Woo

National Aeronautics and
Space Administration
Ames Research Center
Moffett Field CA 94035

January 15, 1992

# THE UNIVERSITY OF MICHIGAN

Radiation Laboratory
Department of Electrical Engineering
and Computer Science
Ann Arbor, Michigan 48109-2122
USA

Report Title:          Electromagnetic Characterization of Conformal
                       Antennas

Primary University Collaborator:    John L. Volakis


Primary NASA-Ames Collaborator:  Alex Woo


University Address:          Radiation Laboratory
                             Department of Electrical Engineering
                               and Computer Science
                             The University of Michigan
                             Ann Arbor MI 48109-2122


Date:                    January 10, 1992

## OBJECTIVE

The ultimate objective of this project is to develop a new technique which permits an accurate simulation of microstrip patch antennas or arrays with various feed, superstrate and/or substrate configurations residing in a recessed cavity whose aperture is planar, cylindrical or otherwise conformed to the substructure. The technique combines the finite element and boundary integral methods to formulate a system suitable for solution via the conjugate gradient method in conjunction with the fast Fourier transform. The final code is intended to compute both scattering and radiation patterns of the structure with an affordable memory demand.

## PROGRESS SUMMARY

This report contains four documents which represent our progress over the past six months. In summary, we continue to improve and develop our original code for other applications and we have begun the development of a new formulation and associated code for cylindrically conformal antennas/arrays. As stated in the included reports the array code developed last year was modified to permit modeling of resistive cards, patch coatings and several new feed configurations, including striplines and aperture coupled feeds. Using these new capabilities we examined the RCS, input impedance, gain and resonant frequency of several rectangular configurations using different loading and substrate/superstrate configurations.

For the development of the new antenna code as applied to cylindrical arrays we require use of new discretization elements and expansion basis. One of the included reports in this binding describes the required elements and we are currently proceeding with the implementation of a formulation based on these elements.

## TRANSITIONS

Over the next six months we shall concentrate on the development and validation of the code for antennas/arrays on a cylindrical surface. We shall also investigate efficient methodologies for extending this analysis to doubly curved conformal arrays. Further improvements and applications of the planar array code are also planned.

# RCS Reduction of a Microstrip Patch Using Lumped Loads

John L. Volakis and Angelos Alexanian

## Abstract

In this report we consider the RCS of a single rectangular patch antenna in a recessed cavity. Using a previously developed finite element-boundary integral code, a study is performed on the patch's RCS as a function of frequency. To reduce the RCS of the patch at the resonant frequency, lumped (resistive) loads are placed at the edges of the patch. The effect of the lumped loads on the patch's RCS and gain are examined and it is observed that the RCS and gain are reduced as the load value decreases, whereas the antenna's bandwidth is increased. At resonance, the usual relation between RCS and gain is observed, but it is shown that this relation no longer holds at frequencies away from resonance.

## Investigation's Scope

The purpose of this study is to (see figure 1):

- Study the RCS vs. Gain of the microstrip antenna by placing lumped resistive loads at the side aperture of the patch

- Determine the resonant frequency shift due to loading

- Assess bandwidth enhancement due to loading

This study was performed by using the University of Michigan program CAV-ITY3D (see Appendices). Other schemes for reducing the RCS of the patch and cavity edges using R-cards and dielectric coating are illustrated in figures 1 and 2, but these have not yet been considered.

## Description of Investigation

To assess the effect of lumped loads on the RCS and Gain of the microstrip patch we considered a 5cm × 3.4cm rectangular patch whose discretized form is shown in figure 3. This patch is loaded with four resistors placed roughly at the midpoint of each side as shown in figures 2 and 3. The thickness of the substrate/cavity was 0.17558cm and the relative dielectric constant was chosen to be $\epsilon_r = 2.17$. Also, for input impedance and gain computations the probe feed was placed at the bottom left corner of the patch as shown in figure 3.

For the above patch, the resonant frequency was found to be $f_0 = 1.94675$GHz with the resistance of each load set at $1500\Omega$ (essentially unloaded). At this frequency we proceeded to evaluate the Gain and RCS of the patch as the resistance was changed from $1500\Omega$ down to zero Ohms (shorted). The normalized values of these quantities as a function of load resistance are plotted in figure 4 and it is clear from this data that the RCS reduction is twice (in dB) that of the Gain (the RCS in figure 4 was computed with no load at the feed). This is to be expected since the RCS at resonance is given by [1]

$$\sigma(\theta, \phi) = \frac{\lambda^2}{\pi} \left\{ G'(\theta, \phi) \right\}^2$$

or

$$10 \log \sigma(\theta, \phi) = 2 \left\{ 10 \log[G'(\theta, \phi)] + 10 \log[\lambda/\sqrt{\pi}] \right\}$$

2

where $10 \log G'$ is the Gain in dB and includes any losses due to lumped or distributed loads. Let us assume that for a given load #1, the Gain is $G'_1$ and for another load #2, the Gain is $G'_2$. The corresponding cross sections evaluated at the same frequency are then given by

$$10 \log \sigma_1 \;=\; 20 \log G'_1 + 10 \log \frac{\lambda}{\sqrt{\pi}}$$

$$10 \log \sigma_2 \;=\; 20 \log G'_2 + 10 \log \frac{\lambda}{\sqrt{\pi}}$$

Subtracting these equations we obtain

$$\Delta\sigma_{\mathrm{dB}} = 10(\log \sigma_1 - \log \sigma_2) = 2[10 \log G_1 - 10 \log G_2]$$

or

$$\Delta\sigma_{\mathrm{dB}} = 2[G_{1\mathrm{dB}} - G_{2\mathrm{dB}}] = 2\Delta G_{\mathrm{dB}}$$

which clearly shows that the dB RCS reduction is twice the dB gain reduction.

As expected, the input impedance becomes reactive with the addition of lumped loads and furthermore its real part is reduced in parallel with the lumped loads. Thus the patch's resonant frequency changes with the value of the applied load. The specific values are illustrated in figure 5 and the reason for the input resistance's reduction is that the lumped loads placed between the patch edges and the ground are in a parallel arrangement with the impedance originally observed at the feed. However, we note that the radiation patterns are essentially unaffected by the placement of the loads (see figures 6(a) and 6(b)). More specifically, the radiation pattern corresponding to the 300$\Omega$ loads is completely identical to that associated with the unloaded patch. We will thus choose to retune the patch with this load placed at its four side apertures (in actuality only the loads at two of the apertures are of significance since the field at the midpoint of the other two vanishes when the patch is at resonance).

The resonant frequency (the frequency at which the input impedance is real) with the feed at the lower left corner ($x = 1.25$, $y = 0.85$ position) of the patch and with the 300$\Omega$ loads at the patch edges was found to be $f_0 = 1.97\mathrm{GHz}$. As given in figure 7 the input resistance at this frequency is approximately 103.5$\Omega$, and as shown in this figure, the input impedance

3

changes rather substantially as the feed position changes. Interestingly, when the feed is at ($x$ = 2.5cm, $y$ = 1.7cm), the input impedance is again real and equal to approximately 49$\Omega$, a value which matches the characteristic impedance of common coaxial cables. From fig. 7, it is also observed that the gain is essentially unaffected by the feed's position implying that the radiation pattern is also unaffected.

With the feed at ($x$ = 2.5cm, $y$ = 1.7cm) and the 300$\Omega$ loads at the patch edges, we next examined the patch VSWR and bandwidth. The results are given in figures 8 and 9, and the assumed source/line impedance was that at $f_0$ = 1.97GHz (i.e., $Z_0 \simeq$ 49$\Omega$). It is seen that the patch bandwidth is increased substantially from fig. 8. Specifically, the bandwidth of the 300$\Omega$ loaded patch is approximately 0.13 (normalized frequency range within which VSWR< 3) whereas that of the unloaded patch is only 0.02 (more than six times smaller). The RCS of the 300$\Omega$ loaded patch in the vicinity of the resonant frequency is shown in figure 10 with or without a load of 49$\Omega$ across the patch at the feed point. As expected, the RCS is maximum at the resonant frequency and then drops rather rapidly away from this frequency. When the 49$\Omega$ load is placed at the feed to simulate the presence of the coax line, a 7dB reduction is observed at the resonant frequency. A more extensive frequency sweep of RCS for different loading configurations can be seen in figure 11. Here we are comparing an unloaded patch to one loaded with four 300$\Omega$ resistors and to another loaded with four 300$\Omega$ along with the 49$\Omega$ at the feed (coax line simulation). Again we observe the expected RCS reduction at the points of resonance.

## Conclusions

One can readily conclude from the above study that the RCS of a patch at resonance can be substantially reduced by placing lumped loads at its side edges. The reduction in RCS achieved in this manner is about twice (in dB) the corresponding reduction in gain. It was also noted that the resonant frequency is a function of the load's value and thus the patch must be retuned for each load. Alternatively, it was shown that the feed location can be moved to again achieve resonance or simply to find an input resistance that matches that of the feeding line.

## Future Study

During the next month we shall investigate the RCS and gain of the patch when a dielectric coating is placed on its upper surface. Also the effect of a uniform R-card across the aperture will be studied. For the first case, a modification of the program is required.

# References

[1] David R. Jackson, "The RCS of a Rectangular Microstrip Patch in a Substrate-Superstrate Geometry," IEEE Trans. Antennas and Propagat., AP-38, pp. 2-8, Jan. 1990.

# Appendices

## Gain Calculations from Program Output Parameters

By definition,

$$\text{Gain} = G'(\theta, \phi) = \lim_{r \to \infty} \frac{4\pi r^2 \frac{1}{2Z_0} |E^r(\theta, \phi)|^2}{P_{\text{in}}}$$

where $E^r$ is the radiated field as a function of the spherical angles $\theta$ and $\phi$, $Z_0$ is the free space intrinsic impedance, $r$ is the distance to the observation point and $P_{\text{in}}$ denotes the input power. For a probe feed, we have that

$$P_{\text{in}} = \tfrac{1}{2}VI^* = \tfrac{1}{2}R_{\text{in}}|I|^2 = \tfrac{1}{2}R_{\text{in}},$$

since $I = 1\text{Amp.}$, in which $R_{\text{in}} = Re\{Z_{\text{in}}\}$ is the antenna input resistance. It then follows that

$$G'(\theta, \phi) = \frac{4\pi \left(\frac{r}{\lambda_{\text{cm}}}\right)^2 |E^r(\theta, \phi)|^2}{Z_0 R_{\text{in}}} \lambda_{\text{cm}}^2$$

in which $\lambda_{\text{cm}}$ denotes the wavelength in centimeters. The dB value of this expression is computed as

$$G'_{\text{dB}}(\theta, \phi) = 10\log_{10}\left[4\pi \left(\frac{r}{\lambda_{\text{cm}}}\right)^2 |E^r(\theta, \phi)|^2\right] + 10\log_{10}\left[\frac{\lambda_{\text{cm}}^2}{Z_0 R_{\text{in}}}\right]$$

The first term in this expression is that computed by the program CAVITY3D and is referred to in that program as the radiated power. The second term must therefore be added externally from the computed value of $R_{\text{in}}$ also given by the program.

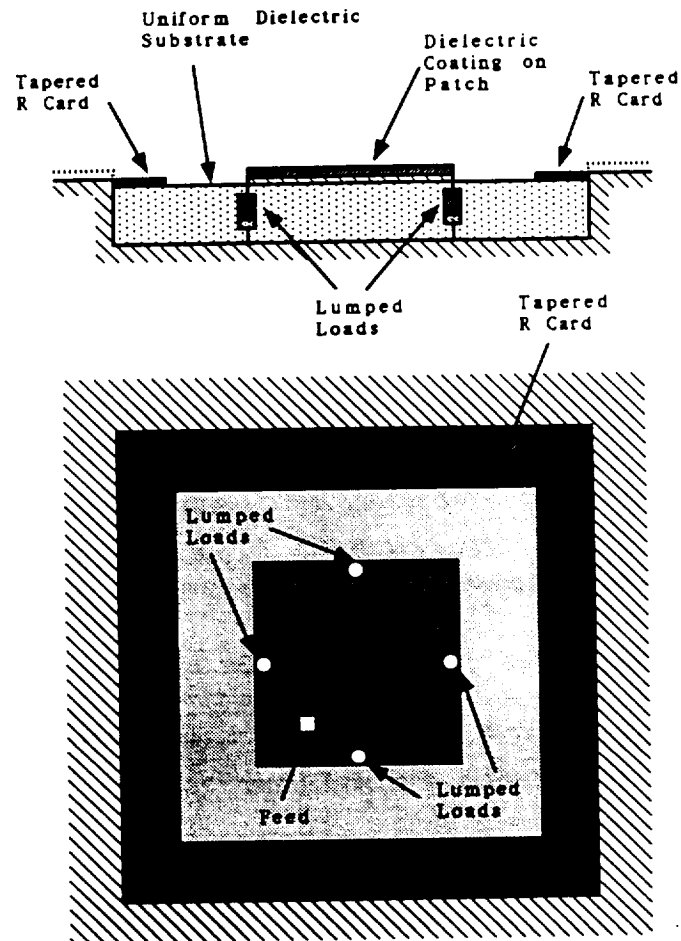## RCS Calculation from Program Output Parameters

The RCS computed by the program CAVITY3D is given in dB above a square wavelength. To obtain the RCS in square meters the following formula must be applied externally:

$$\sigma_{\text{dBSM}} = \sigma_{\text{dBSW}} + 20\log_{10}(\lambda_{\text{m}})$$

where $\lambda_{\text{m}}$ is the wavelength in meters.

-6

# RCS Reduction Studies

- Resistive cards
- Lumped loads
- Shape
- Feed mechanism



- Study RCS vs gain characteristics for various load treatments

- Study resonant frequency shift due to loading

- Study bandwidth enhancement as a function of loading

**Figure 1**

# Other RCS reduction approaches
# for simple elements



Figure showing radiating slot, tapered R card, R card strips, and tuning wires.
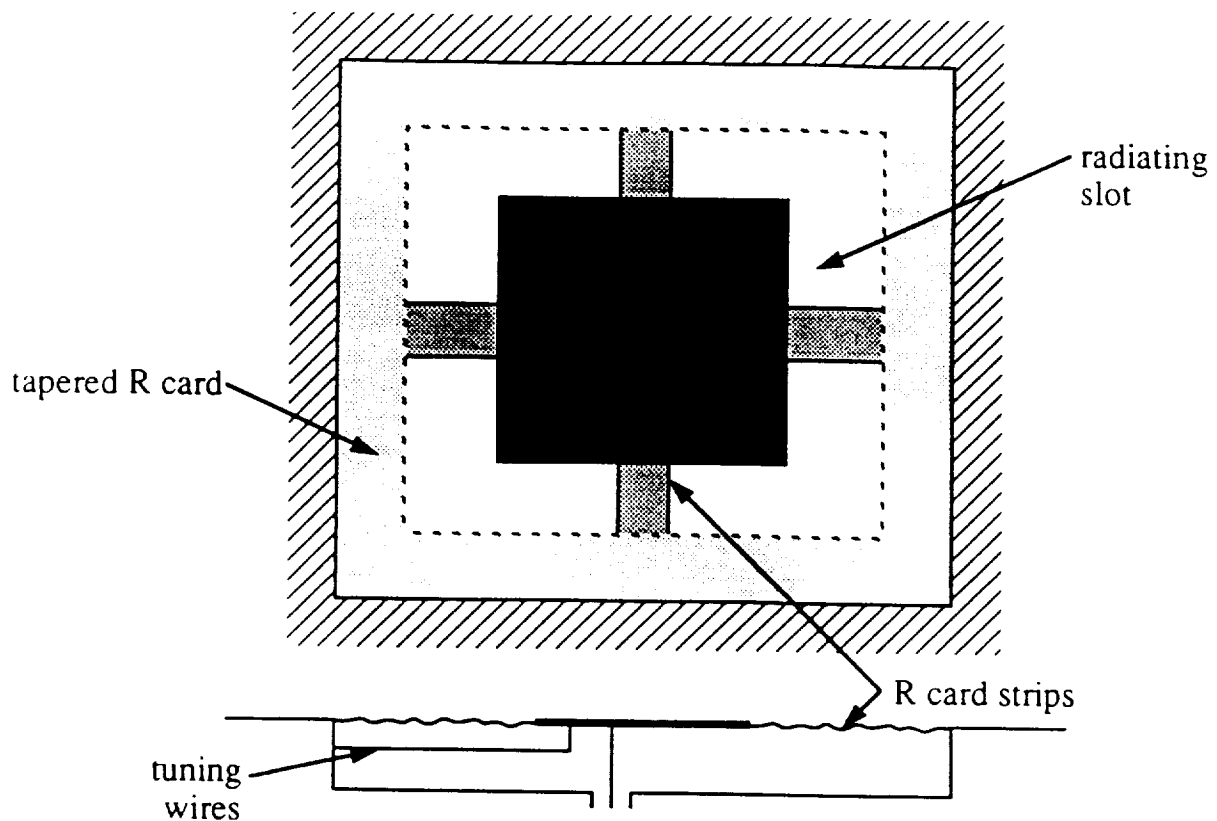
- Tapered R Card reduces RCS of terminations without effecting antenna parameters.

- R Card strips act as lumped loads in reducing the RCS. They reduce RCS and Gain, but RCS is usually reduced much more.

- Patch must be retuned after loading.

- Radiation pattern is generally uneffected.

- Surface wave effects are suppressed because of cavity enclosure.

Goal: Given certain criteria with respect to Gain, bandwidth, and RCS at the design frequency, what should be the loading, feed mechanism and structural characteristics of the patch antenna?
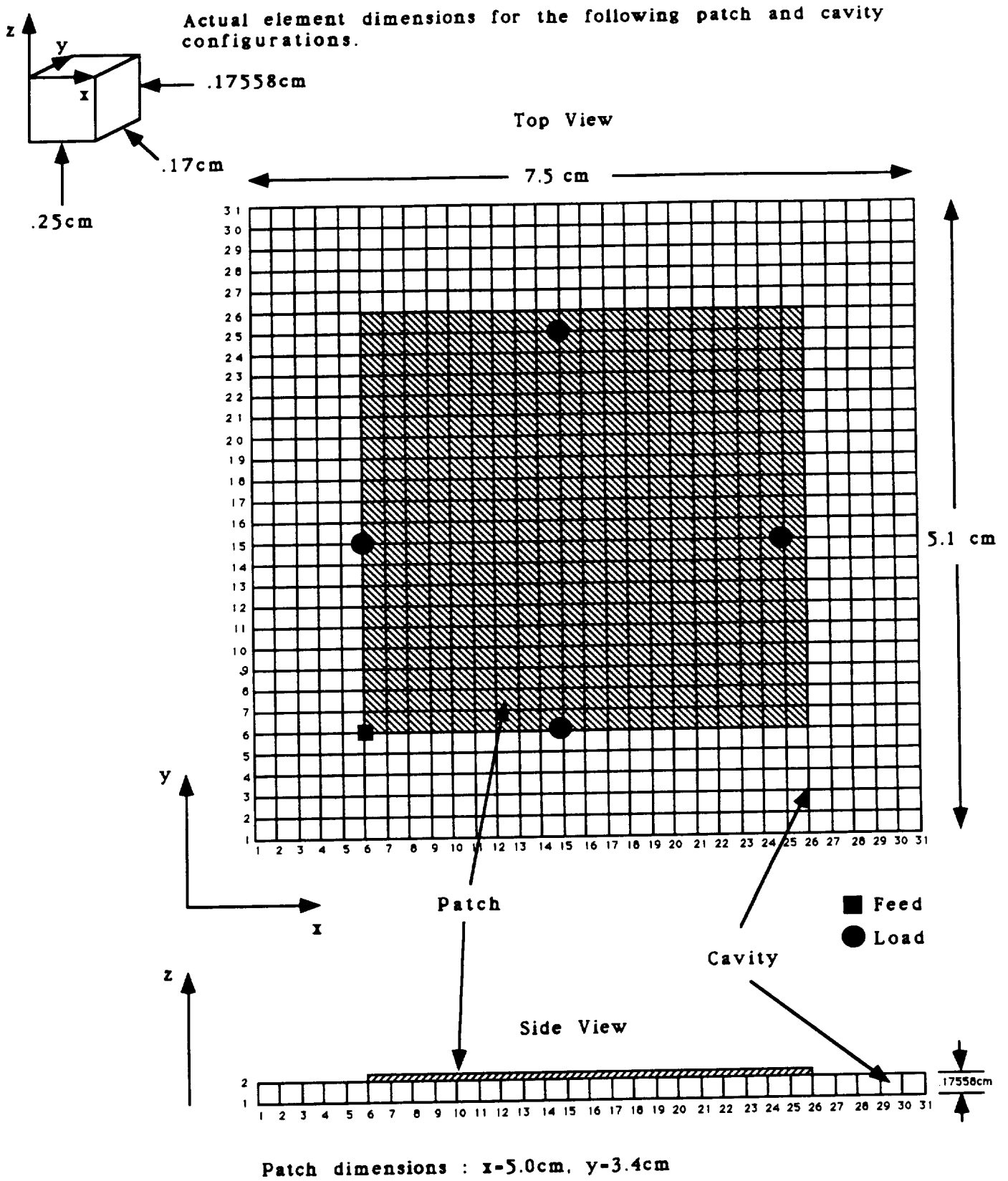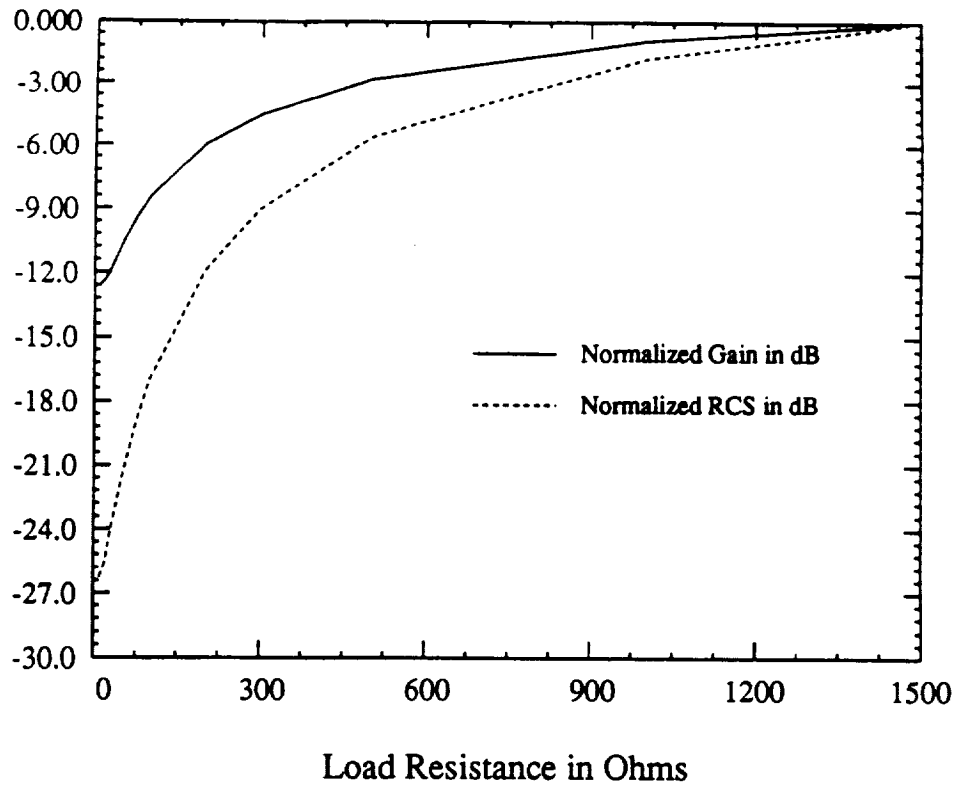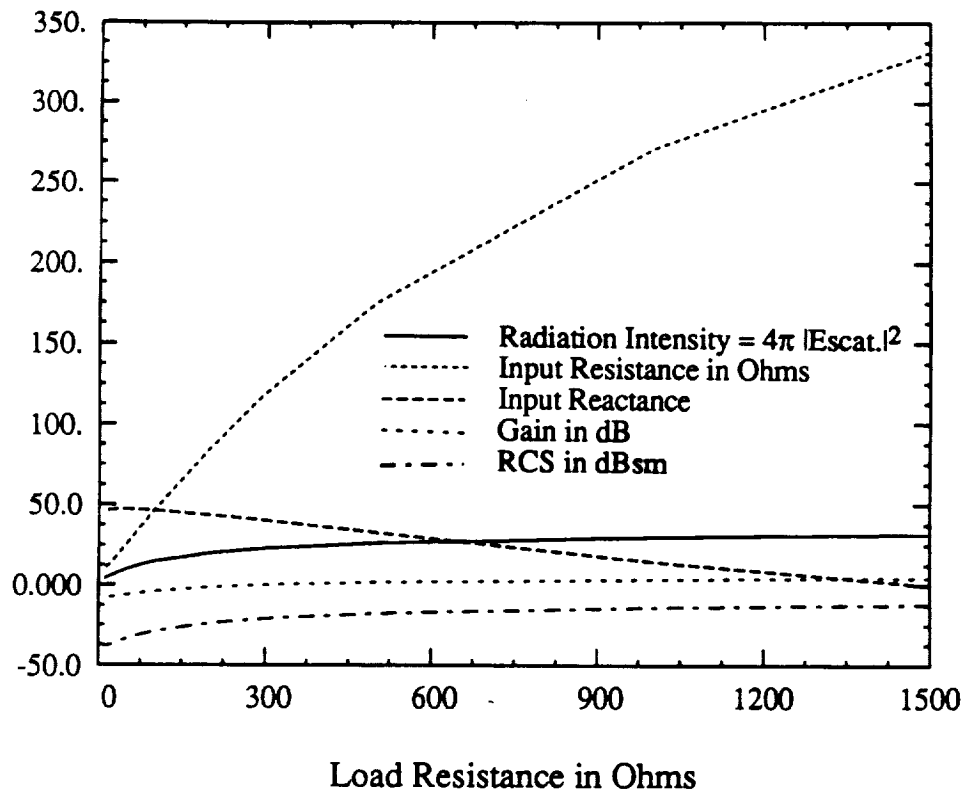
**Figure 2**

Actual element dimensions for the following patch and cavity configurations.

.17558cm

.17cm

.25cm

Top View

7.5 cm

5.1 cm

Patch

Feed
Load

Cavity

Side View

.17558cm

Patch dimensions : x-5.0cm, y-3.4cm

Figure 3

**Figure 4**



**Figure 5**

## Power Patterns (φ=0°)



Load Resistance = 1500 Ohms
Load Resistance = 300 Ohms
Load Resistance = 75 Ohms
Load Resistance = 20 Ohms
Load Resistance = 10 Ohms

Angle θ in degrees

**Figure 6(a)**

## Power Patterns (φ=90°)



Load Resistance = 1500 Ohms
Load Resistance = 300 Ohms
Load Resistance = 75 Ohms
Load Resistance = 20 Ohms
Load Resistance = 10 Ohms

Angle θ in degrees
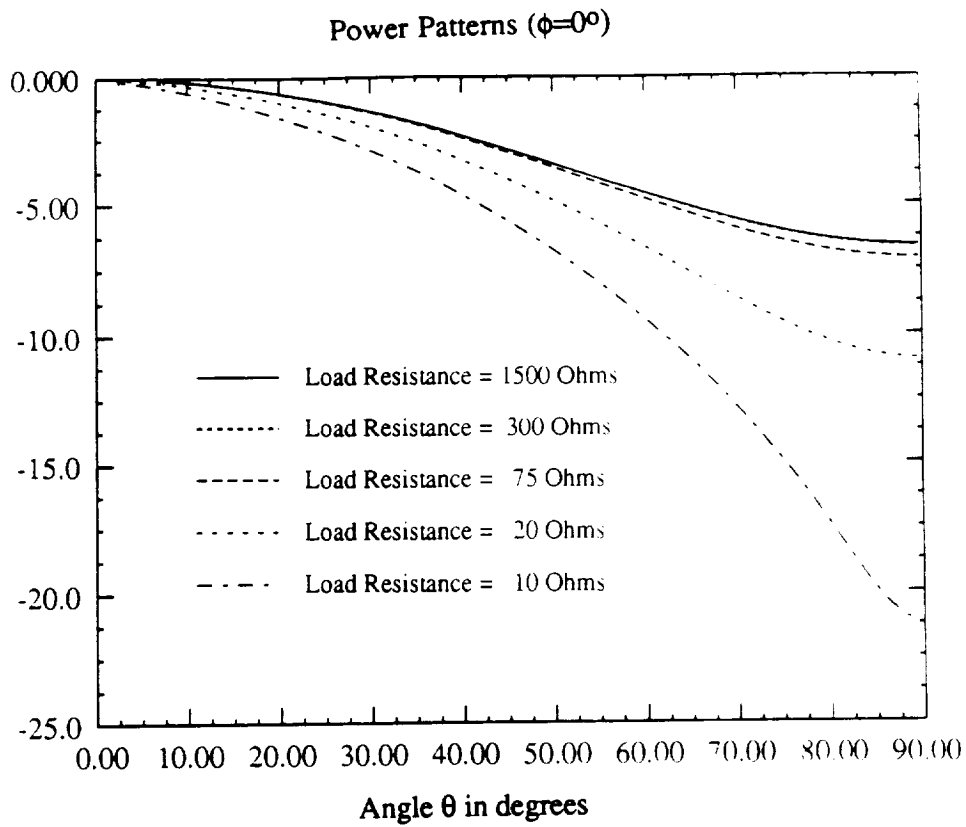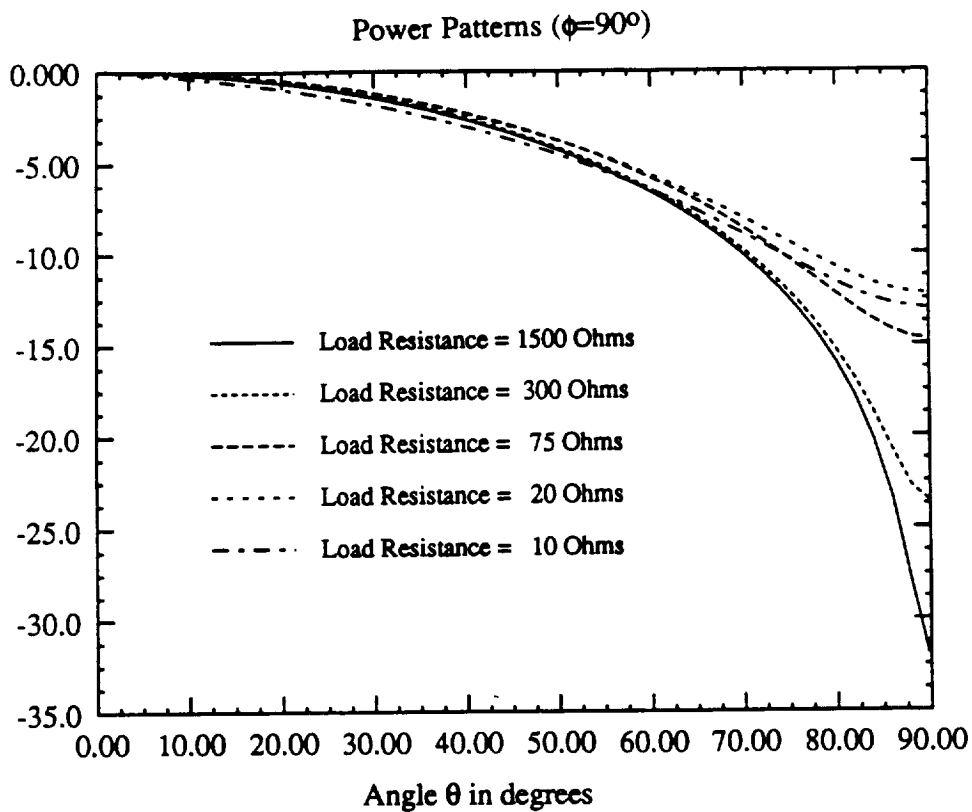
**Figure 6(b)**

Radiation Properties of Patch as Feed is Moved

Legend:
- Radiation Intensity = $4\pi |Escat.|^2$
- Input Resistance in Ohms
- Input Reactance
- Gain in dB

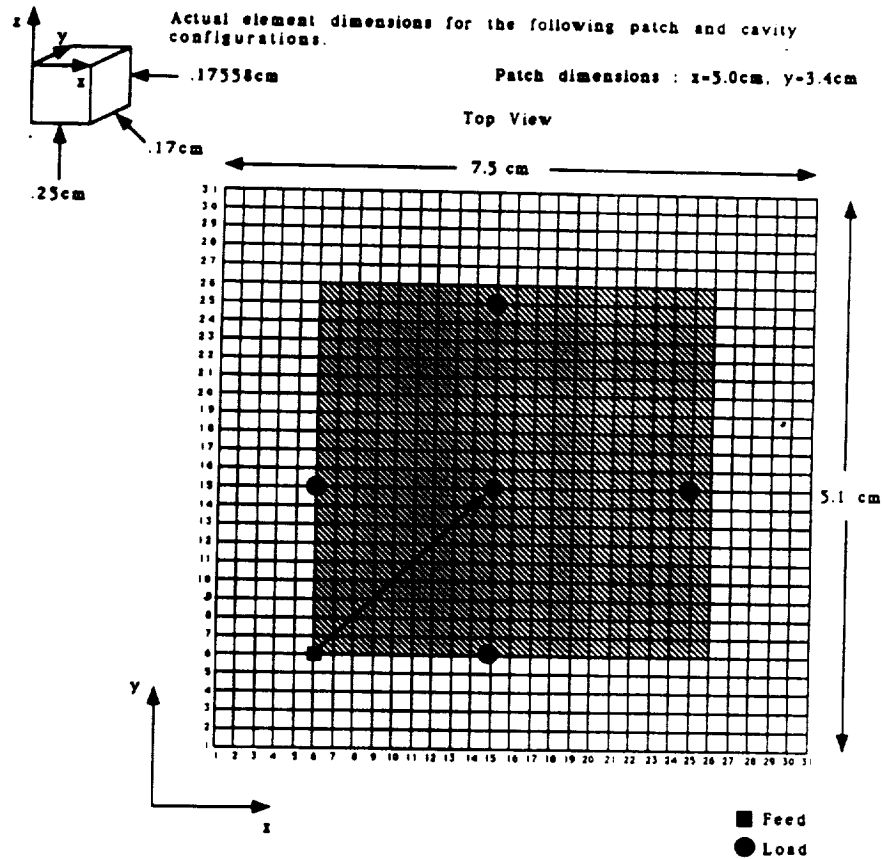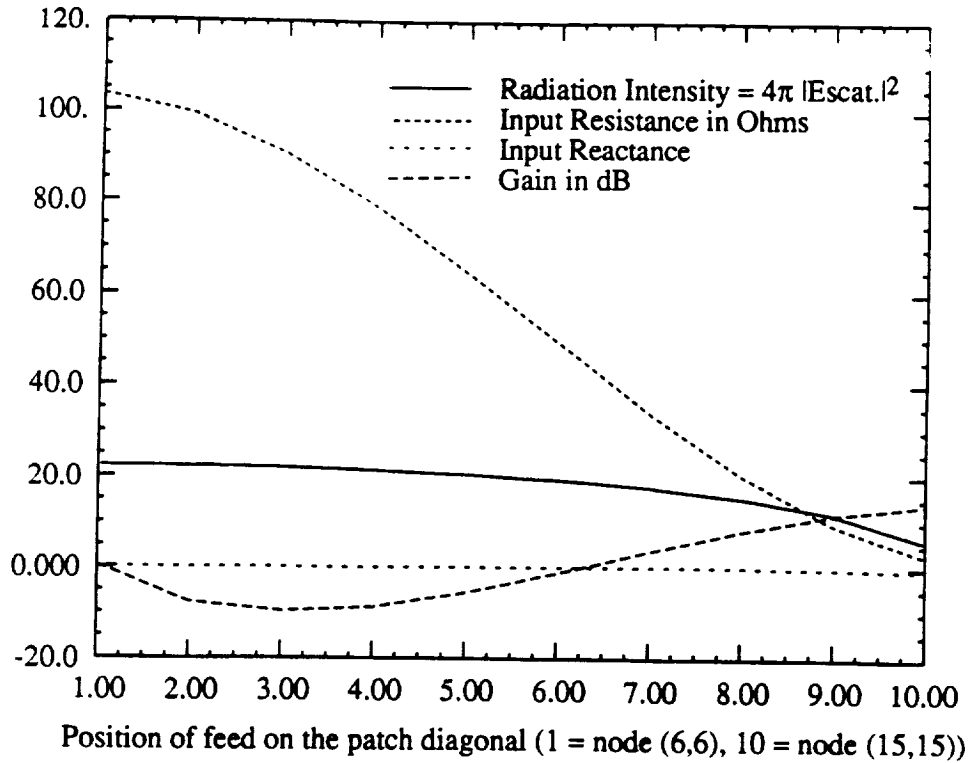Position of feed on the patch diagonal (1 = node (6,6), 10 = node (15,15))

**Figure 7.** The arrow on the patch above indicates the motion of the feed with initial and final positions at nodes (6,6) and (15,15) respectively. The frequency is 1.97GHz which happens to be the resonant frequency for four $300\Omega$ loads and the feed at node (6,6). With the feed at node (11,11) it is interesting to note that the input impedance becomes approximately $50\Omega$ (ie. $48.92 - j1.13 \, \Omega$).
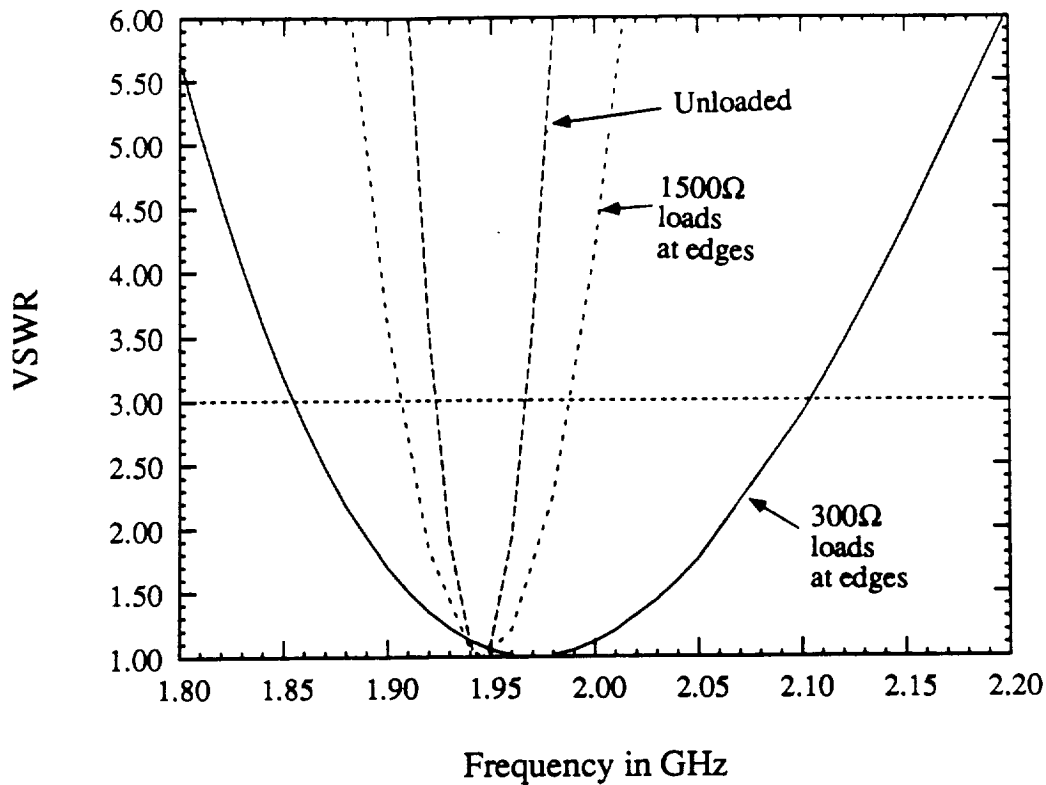
VSWR

6.00
5.50
5.00
4.50
4.00
3.50
3.00
2.50
2.00
1.50
1.00

1.80  1.85  1.90  1.95  2.00  2.05  2.10  2.15  2.20

Unloaded

1500Ω
loads
at edges

300Ω
loads
at edges

Frequency in GHz

**Figure 8.** VSWR of loaded and unloaded patch vs frequency

Computation of VSWR :

VSWR = (1+|Γ|)/(1-|Γ|)     where   Γ = (Zin-Zinr)/(Zin+Zinr)

Zinr= 48.92-j1.13 Ω is the input impedance at the resonant frequency (1.97GHz) for four 300Ω loads and feed at node position (11,11). Note that at this frequency VSWR=1.

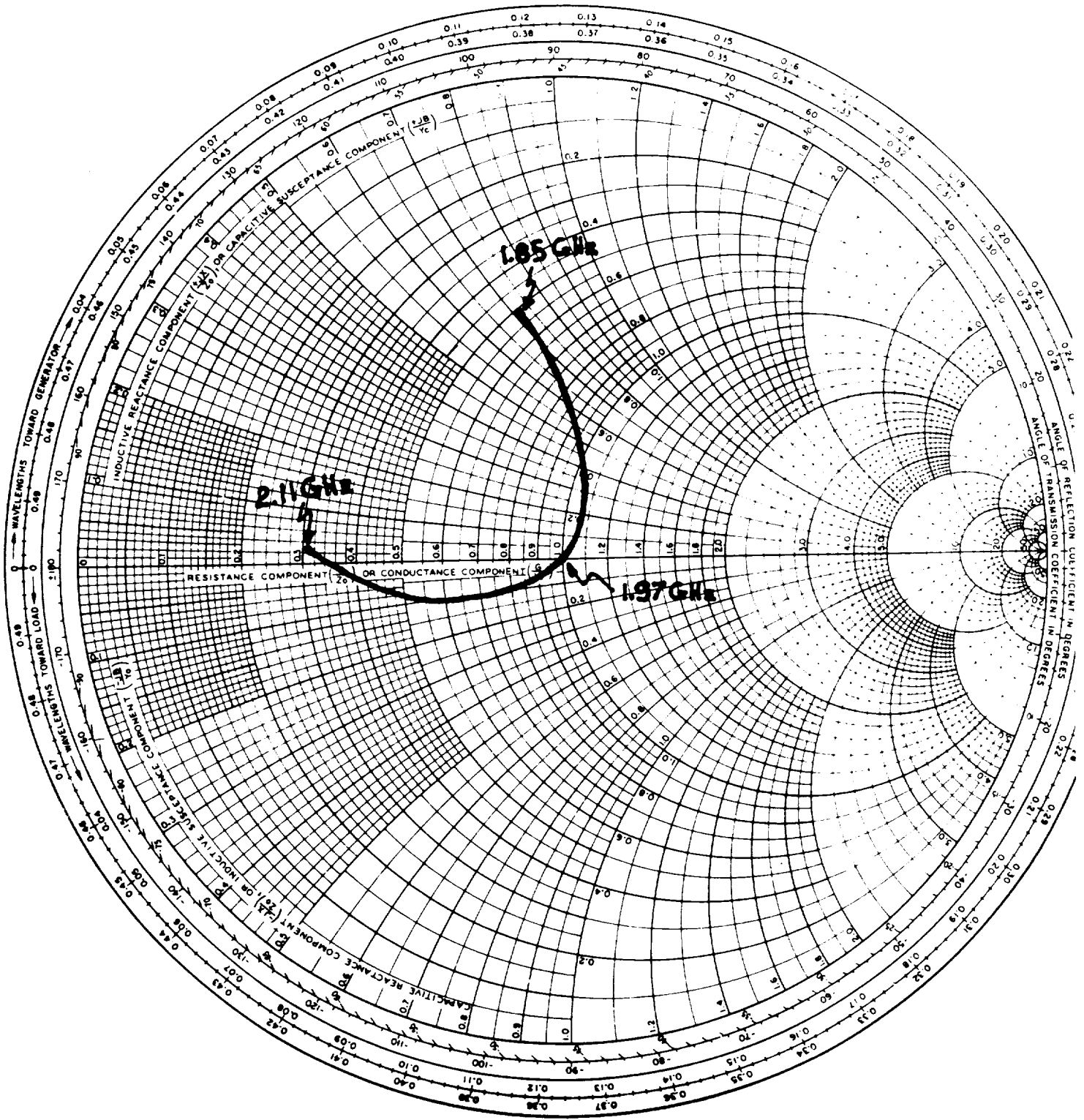Zin = input impedance for the same configuration as above, with the exception that the frequency varies.

**Figure 9.** $\Gamma$ (as defined in figure 8) vs frequency on a smith chart. Note that the endpoints of this graph correspond to VSWR=3.
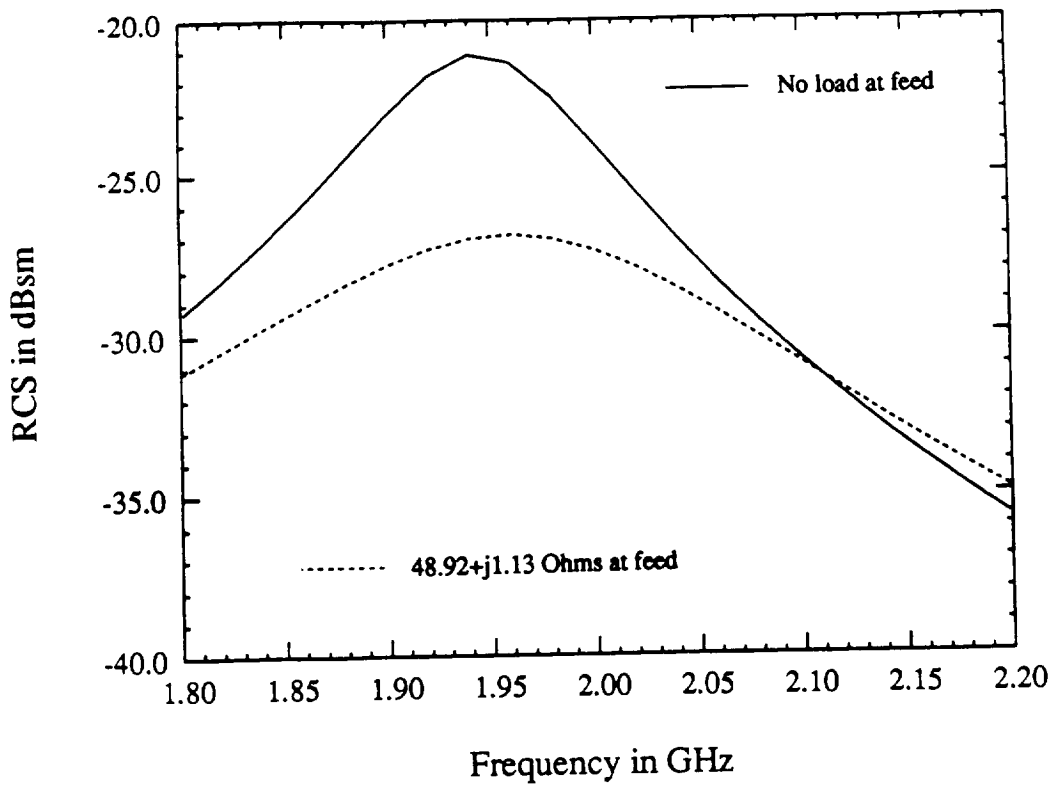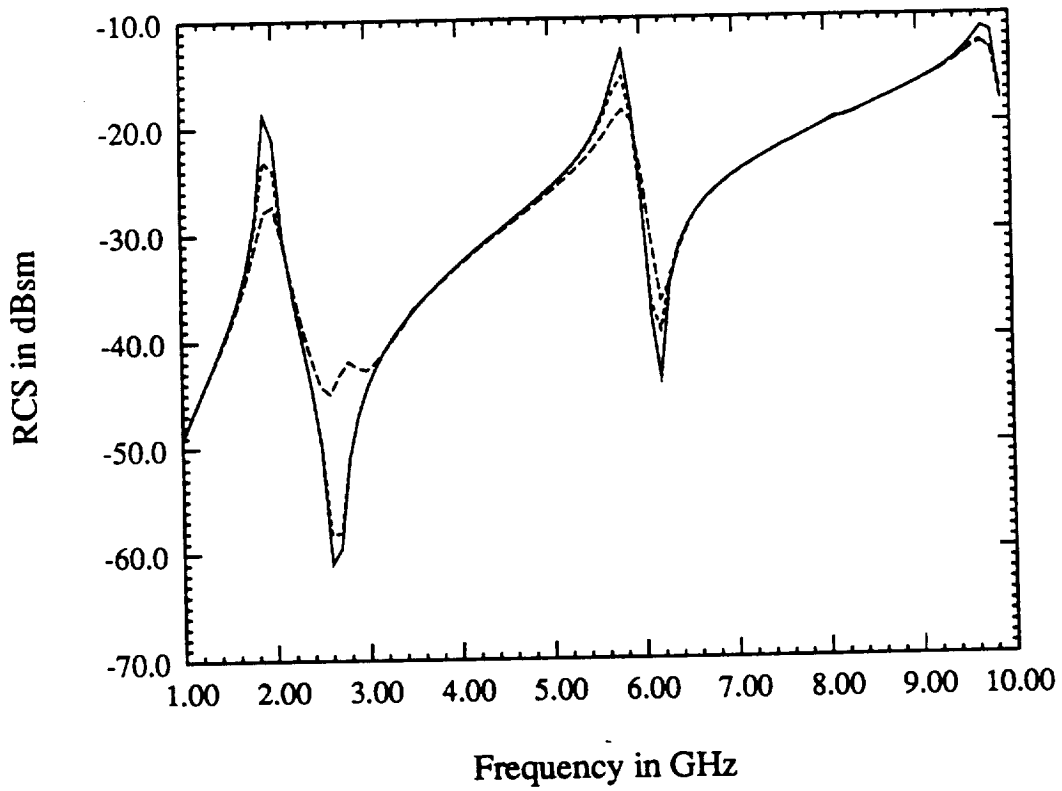
**Figure 10.** RCS as a function of frequency



**Figure 11.** RCS as a function of frequency

## Typical input file

| | |
|---|---|
| 7.5 5.1 .17558 | cavity size in cm (x,y,z) |
| 31 31 2 | number of nodes (x,y,z) |
| 1 | - uniform dielectric |
| (2.17,0) (1.,0.) | substrate dielectric - εr μr |
| 1.97 1.97 1 | frequency min, max, increment |
| 2 | - radiated intensity calculation |
| 0 0 1 | theta min, max, increment |
| 0 0 1 | phi min, max, increment |
| .01 800 | tolerance, number of iterations |
| 2 | - monitor cnvergence 1=yes 2=no |
| 1 | number of patch |
| 6 6 | lower left corner of patch node(x,y) |
| 20 20 | number of elements on patch (x,y) |
| 1 | layer in which patch resides |
| 2 | - patch display 1=yes 2=no |
| 0 | number of short circuit pins |
| 1 | number of feeds |
| 11 11 | feed position node(x,y) |
| 1 0 | amplitude and phase of current source |
| 1 | layer in which feed is embedded |
| 4 | number of loads |
| 15 6 | node(x,y) load 1 position |
| (300.,0.) | value of load 1 (complex) in Ω |
| 1 | layer in which load 1 is embedded |
| 25 15 | node(x,y) load 2 position |
| (300.,0.) | value of load 2 (complex) in Ω |
| 1 | layer in which load 2 is embedded |
| 15 25 | node(x,y) load 3 position |
| (300.,0.) | value of load 3 (complex) in Ω |
| 1 | layer in which load 3 is embedded |
| 6 15 | node(x,y) load 4 position |
| (300.,0.) | value of load 4 (complex) in Ω |
| 1 | layer in which load 4 is embedded |
| 2 | - resistive card 1=yes 2=no |

**Figure 12**

Actual element dimensions for the following patch and cavity configurations.

.17558cm

.17cm

.25cm

Top View

7.5 cm

5.1 cm

■ Feed
● Load

Side View

.17558cm

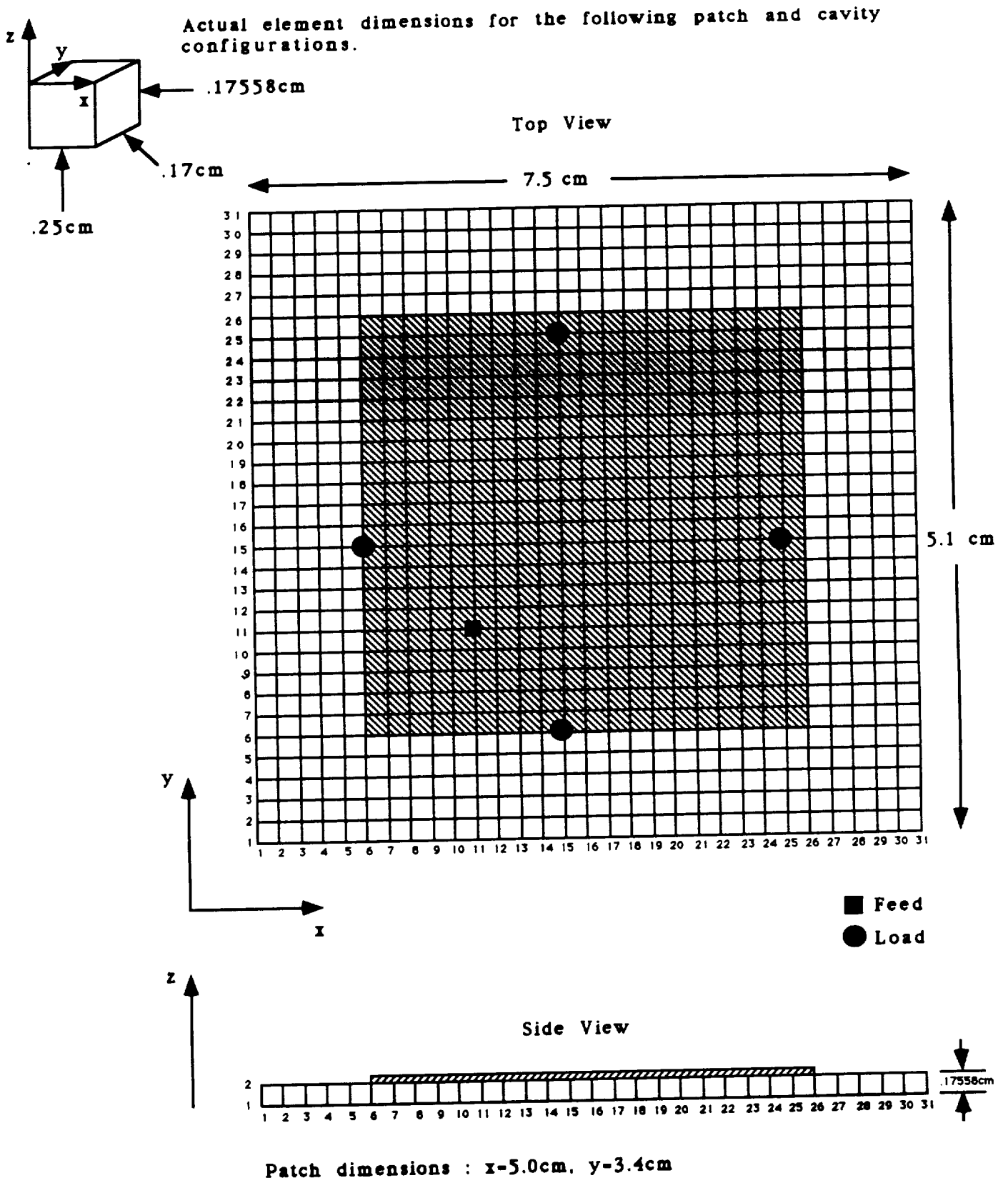Patch dimensions : x-5.0cm, y-3.4cm

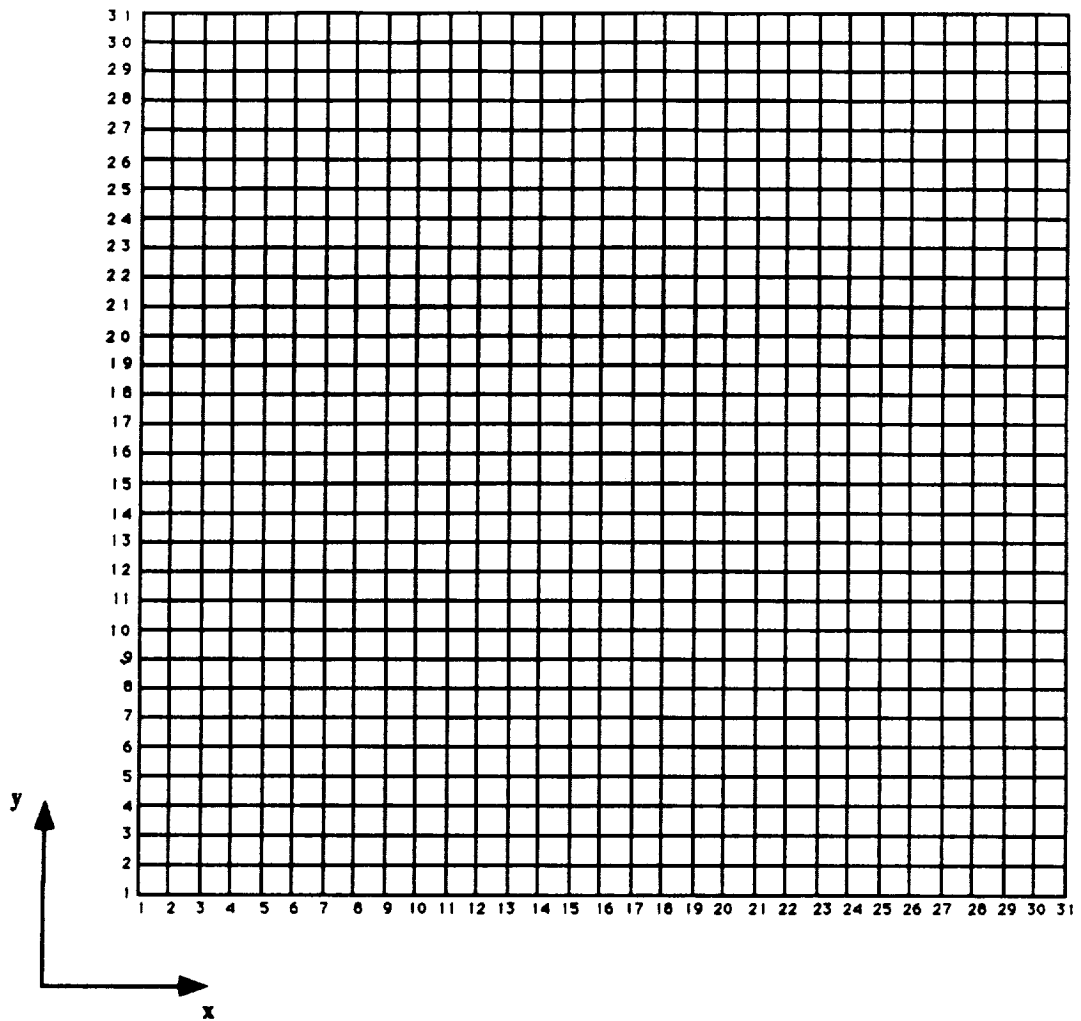**Figure 13.** This is the exact patch-cavity configuration resulting from the input file given in figure 12.

**Figure 14.** Extra grid for future designs.

# A scheme to alter the resonant frequency
# of the microstrip patch antenna

J. L. Volakis and J. M. Jin

December 20, 1991

**Abstract**

Simple schemes are presented for altering the resonant frequency of the rectangular patch antenna without a need to change its size. In particular, by placing a perturbance below the patch it is shown that as much as 20 percent increase and 30 percent decrease from the resonant frequency of the unperturbed patch can be achieved. The specific configurations considered in this letter include a cavity-backed, aperture-backed and a protrusion-backed patch, and for each case design curves are presented.

## Introduction

In many cases one is required to design a certain antenna or array which does not exceed given physical dimensions. Since the size of the antenna is typically determined by its operational frequency, restrictions on the physical dimensions of the antenna can present a challenge to the antenna designer. To facilitate the design process, in this letter we consider simple schemes to rather substantially lower or increase the operational frequency of the rectangular microstrip patch antenna without altering its aperture size. These include the placement of some perturbance (protrusion, depression or slot) in the cavity region below patch, a scheme well known to designers for controlling the cavity's resonant frequency [1], [2] or other antenna parameters [3]. However, because of a lack of available CAD tools to treat such perturbances, the approach does not appear to have been explored for altering the

1

frequency of the highly resonant microstrip antennas. Moreover, traditional applications of these frequency control methods dealt with small shifts in the resonant frequency.

Recently, a new analytical technique was developed for a characterization of microstrip antennas or arrays residing in a cavity that is recessed in a ground plane [4]. The technique is based on a hybrid version of the finite element method (FEM) where the mesh is terminated at the aperture of the patch via the exact boundary integral equation. Because of the FEM's geometrical adaptability perturbances or irregularities in the cavity's geometry, and material inhomogeneities in the substrate can be modeled without difficulty. Below we specifically consider the effect of three different cavity configurations on the resonant behavior of a given patch residing at the aperture of the cavity.

## Antenna Geometry

Consider the reference geometry illustrated in Fig. 1. The configuration consists of a square 4.45cm × 4.45cm patch residing in a square cavity whose aperture size is 6.625cm × 6.625cm and depth is .05cm. The cavity is filled with a dielectric having a relative permittivity of $\epsilon_r = 2.17$ and we remark that its finite size has negligible effect on the resonance and input impedance of the patch.

With the goal of altering the resonant behavior of this patch we consider three modifications of the cavity. The $xz$ and $yz$ cross sections of these are illustrated in Fig. 2(a)-(c). They include a rectangular depression at the center of the original cavity, a second cavity which is aperture coupled to the original and a third configuration having a rectangular protrusion below the patch. In all cases the patch and aperture size is unchanged from the original antenna shown in Fig. 1.

The analysis of all four patch antennas depicted in Figs. 1 and 2 was accomplished via the hybrid finite element-boundary integral (FE-BI) method described in [4]. In accordance with this method the cavity region below the patch is formulated via the finite element method, which is readily adaptable to any cavity configuration with an appropriate choice of element shapes. For the particular cavity geometries at hand we employed rectangular bricks with edge-based shape functions which have zero divergence and are appropriate for modeling metallic corners. Because the FEM solves the wave equation, it

yields a solution subject to the boundary conditions at the cavity walls and its aperture. For our case, the tangential field is set to zero at the interior cavity walls and at the aperture we enforce the field continuity between the interior and exterior fields. The last fields are expressed in terms of the radiation integral with the sources set equal to the tangential aperture fields. Consequently, the continuity condition on the aperture fields results in an integral equation which can be alternatively thought as a global mesh termination condition. In contrast to the usual absorbing boundary condition(s) which must also be enforced far from the radiating element, this approach is exact but involves a partially full submatrix. However, by solving the resulting (sparse) system via the biconjugate gradient method the need to generate the matrix is eliminated thus retaining the $O(N)$ storage requirement, which is typical in FEM solutions. As noted in [4] we have found this solution approach to be highly efficient with respect to the system size and convergence rate.

## Numerical Results

Plots of the resonant frequency associated with the configurations in Figs. 2(a) and 2(b) to be referred to as cavity-backed or aperture-backed antennas, respectively, are given in Figs. 3 and 4. In Fig. 3, we depict the resonant frequency as a function of the second (bottom) cavity depth with the aperture at the interface of the two cavities fixed at 3.56cm × 3.56cm. The plot in Fig. 4 illustrate the effect of the aperture size on the resonant frequency with the bottom cavity depth kept at 0.3cm. From both figures, it is seen that by changing the aperture or depth of the bottom cavity one can decrease the patch's resonant frequency by as much as 30 percent. Consequently, one may construct a 30 percent smaller patch from the conventional one with the introduction of the second cavity. We have also verified that the RCS of the new antenna structure is nearly the same as that of the original, and thus the new design results in an overall reduction of the antenna's radar cross section (RCS). It should be noted though that when the aperture of the second cavity becomes larger than the patch size, there is minimal frequency shift and this is clearly shown in Fig. 4. The shift in the resonant frequency can be understood by resorting to a transmission line model of the patch antenna. In this case the inserted aperture below the patch can

be represented by an equivalent reactance placed between the admittances representing the patch terminations.

The resonant frequency of the third antenna (protrusion-backed) depicted in Fig. 2(c) is plotted in Fig. 5 as a function of the protrusion's height. For these calculations the $xy$ cross section of the protrusion was fixed to be 3.56cm × 3.56cm. Not surprisingly, the protrusion increases the resonant frequency of the original patch almost linearly and up to 20 percent as the protrusion height is increased. As expected, when the protrusion's cross section extends beyond the patch, there is minimal shift in the resonant frequency of the reference patch having a substrate thickness equal to the distance between the patch and protrusion.

Unfortunately, the bandwidth of the cavity-backed and aperture-backed configurations was not altered although some differences were observed in the actual values of the input impedance as shown in Fig. 6. To increase the patch's bandwidth one could, of course, resort to standard approaches such as those reported in [5],[6]. Some bandwidth increase is observed for the protrusion-backed antenna but this is attributed to the larger substrate thickness below the patch's edges.

# References

[1] A. Parkash, J.K. Vaid, and A. Mansingh, "Measurement of dielectric parameters at microwave frequencies by cavity-perturbation techniques," *IEEE Trans. Microwave Theory and Techn.*, vol. MTT-27, pp. 79–95, Sept. 1979.

[2] P.L. Sullivan and D.H. Schaubert, "Analysis of an aperture coupled microstrip antenna," *IEEE Trans. Antennas and Propagation*, vol. AP-34, pp. 977–984, Aug. 1986.

[3] H. Nakatano, H. Soga, T. Honma and J. Yamauchi, "Effects of adding a small disk to a spiral antenna backed by a conducting plane reflector," *IEE Proceedings-H*, vol. 138, pp. 375–377, Aug. 1991.

[4] J.M. Jin and J.L. Volakis, "A hybrid finite element method for scattering and radiation by microstrip patch antennas and arrays residing in a cav-

4

ity," *IEEE Trans. Antennas and Propagation,* vol. AP-39, pp. 1598–1604, Nov. 1991.

[5] H.K. Smith and P.E. Mayes, "Stacking resonators to increase the bandwidth of low profile antennas," *IEEE Trans. Antennas and Propagation,* vol. AP-35, pp. 1473–1476, Dec. 1987.

[6] L. Barlatey, J.R. Mosig and T. Sphicopoulos, "Analysis of stacked microstrip patches with a mixed potential integral equation," *IEEE Trans. Antennas and Propagation,* vol. AP-38, pp. 608–615, May 1990.
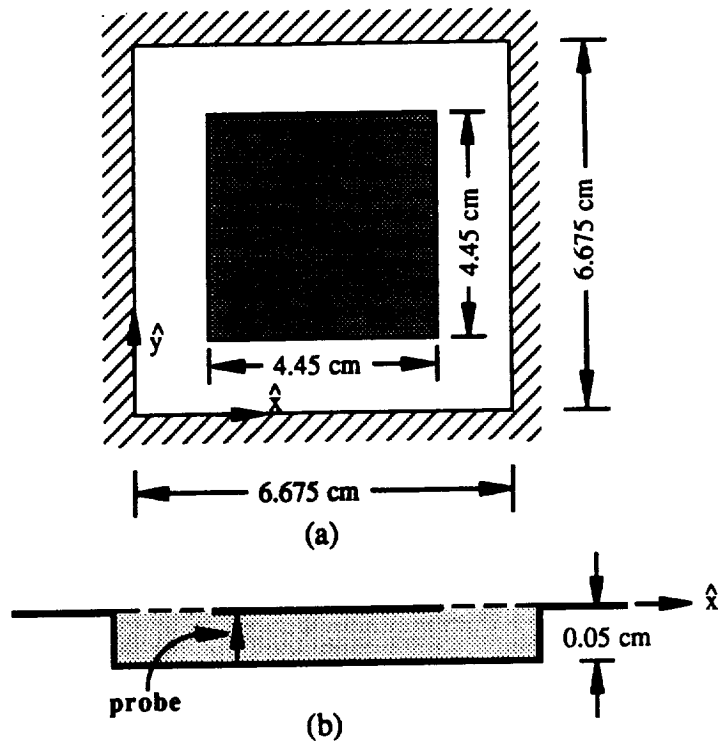
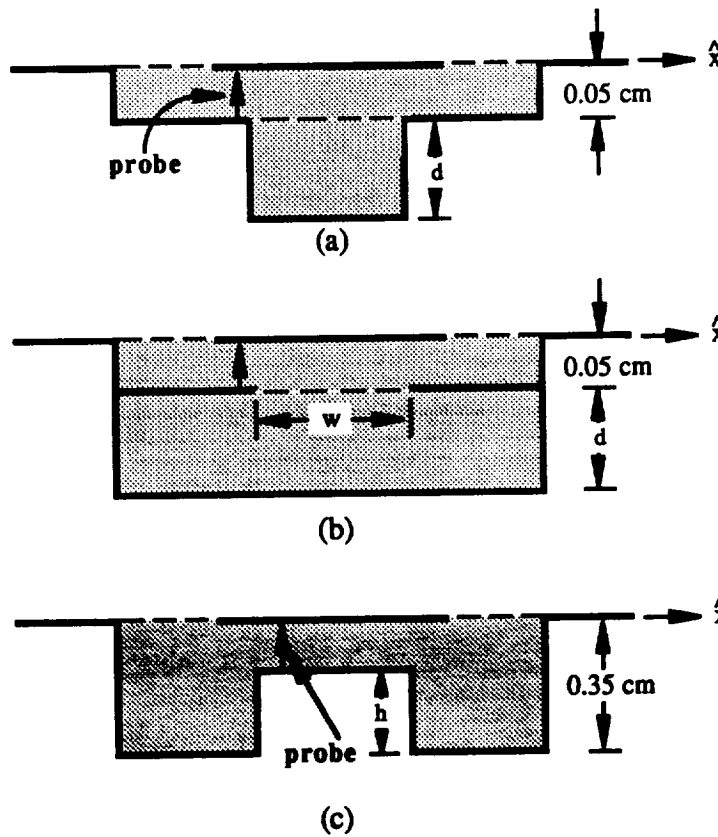Figure 1. Reference geometry of the microstrip patch in a metal-backed rectangular cavity.



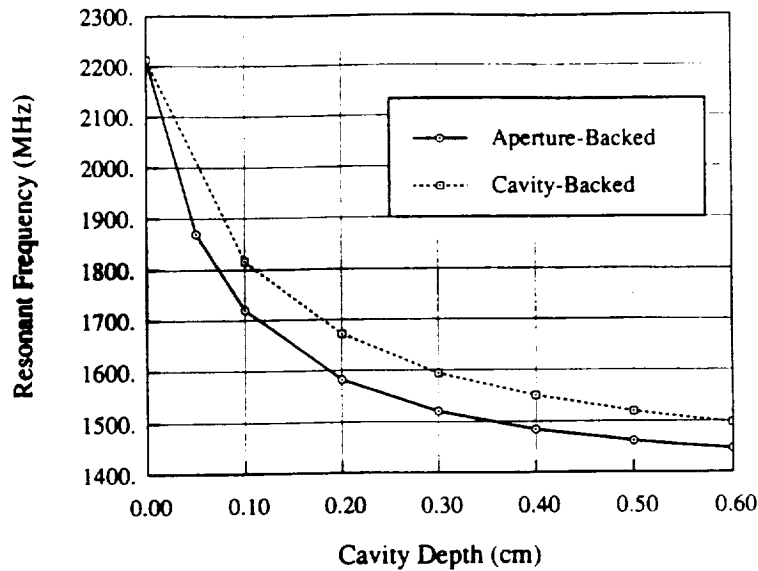Figure 2. Modified cavity configurations: (a) cavity-backed, (b) aperture-backed, (c) protrusion-backed.

Figure 3. Resonant frequency of the aperture- and cavity-backed patch configurations as a function of the bottom cavity depth $d$. The original cavity depth is retained at 0.05cm and the entire cavity region is filled with a dielectric having $\epsilon_r = 2.17$. The aperture of the second cavity is 3.56cm × 3.56cm.
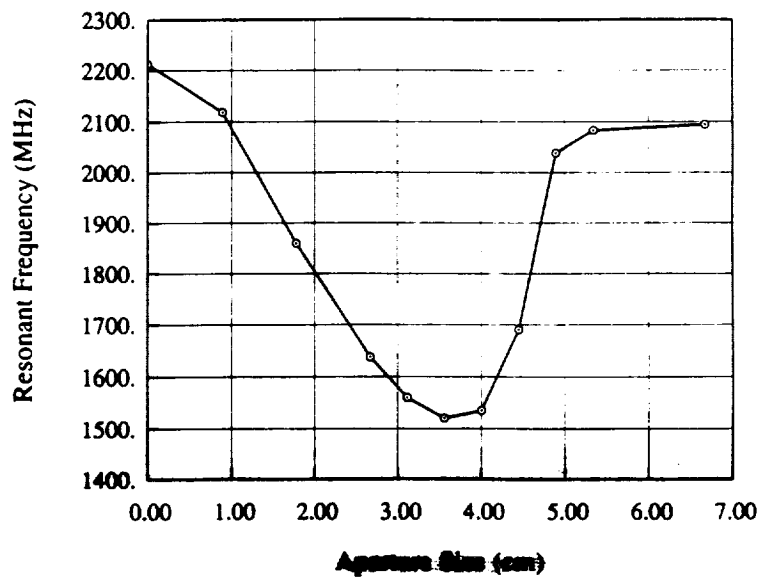


Figure 4. Resonant frequency of the aperture-backed patch as a function of the square aperture dimension $w$. The depth of the bottom cavity was kept at $d = 0.3$cm and all other parameters are the same with those used for Figure 3.
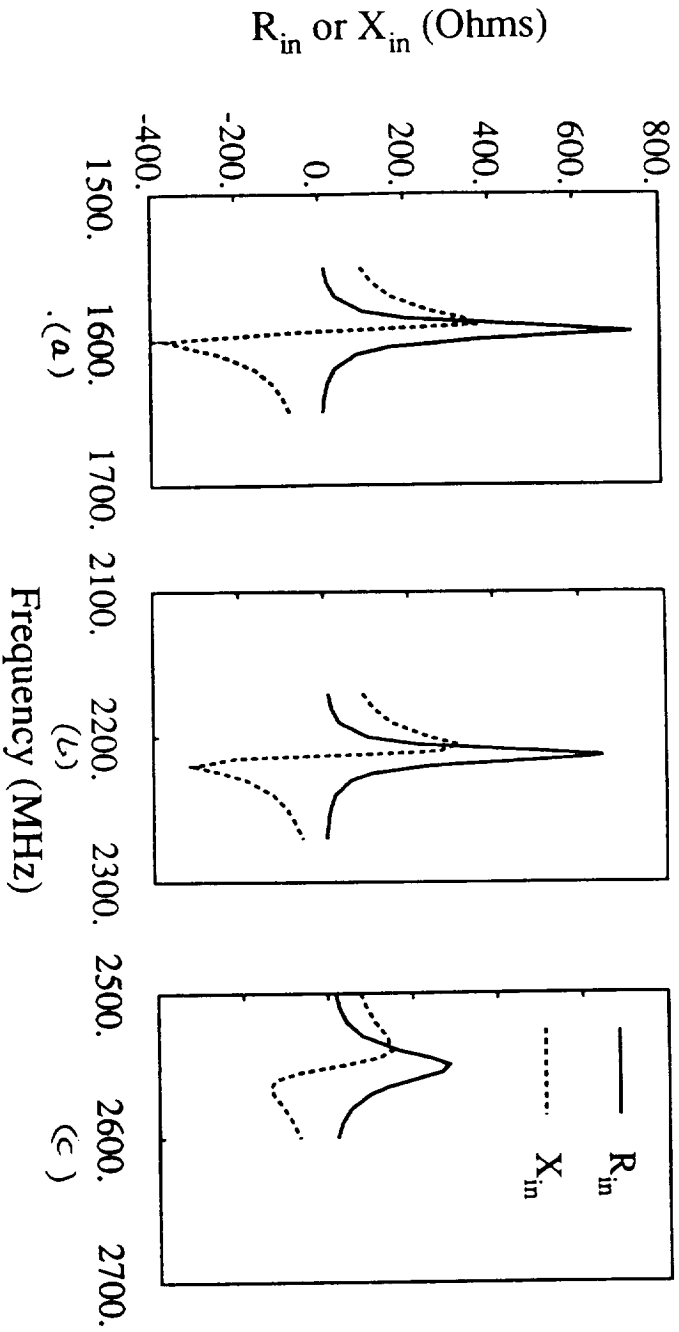
$R_{in}$ or $X_{in}$ (Ohms)

800.
600.
400.
200.
0.
-200.
-400.

1500. 1600. 1700. 2100. 2200. 2300. 2500. 2600. 2700.

Frequency (MHz)

.(a)

(b)

(c)

—— $R_{in}$

········ $X_{in}$

**Figure 6.** **Patch input impedance with the modified cavity configuration: (a) cavity-backed** with $d = 0.3$cm, (b) unperturbed antenna shown in Fig. 1, (c) protrusion-backed with $h = 0.3$cm. For (a) and (b) the probe feed was placed at the diagonal of the patch and 0.315cm from the nearest corner. For (c), the feed was placed at the diagonal of the patch and a distance of 1.259cm from the nearest corner.
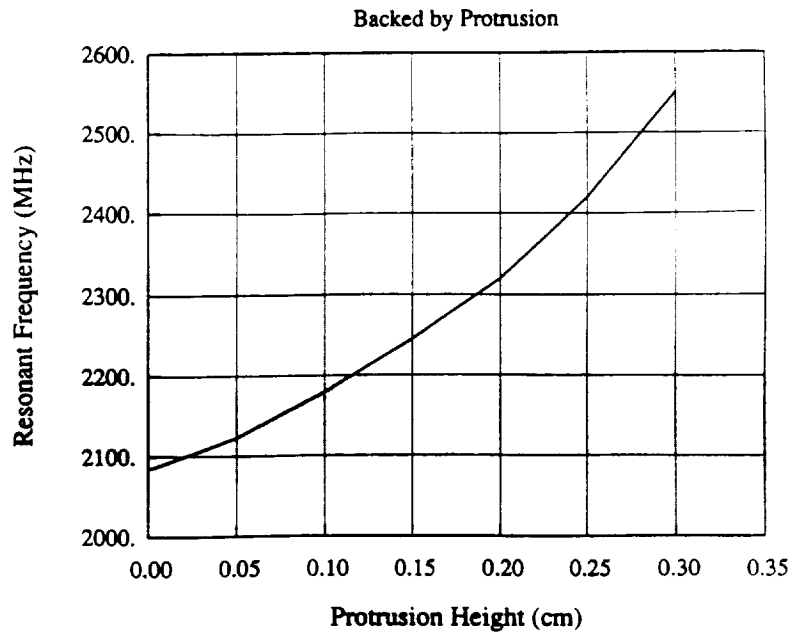
Figure 5. Resonant frequency of the protrusion-backed patch as a function of the protrusion's height $h$. The protrusion's $xy$ cross section was kept at 3.56cm × 3.56cm.

# A Collection of Edge-Based Elements

Leo C. Kempel and John L. Volakis
Radiation Laboratory
University of Michigan

January 5, 1992

### Abstract

Edge-based elements have proved useful in solving electromagnetic problems since they are divergenceless. Previous authors have presented several two-dimensional and three-dimensional elements. Herein, we present four types of elements which are suitable for modeling several types of three-dimensional geometries. Distorted brick and triangular prism elements are given in cartesian coordinates as well as the specialized cylindrical shell and pie-shaped prism elements which are suitable for problems best described in polar cylindrical coordinates.

# Contents

where $\bar{E}$ is the electric field and $G$ is a Green's function. For the remainder of this report, we suppress the dependence of F on the unprimed coordinates since there will be no operations carried out in these coordinates. Furthermore, we express (1) in terms of its cartesian components

$$\bar{I} = \hat{x}I_x + \hat{y}I_y + \hat{z}I_z \tag{3}$$

where

$$I_\zeta = \hat{\zeta} \cdot \int_V \bar{F}(x',y',z')\, dx'\, dy'\, dz' \tag{4}$$

and $\zeta \in \{\, x,y,z\,\}$.

To evaluate (4), we apply the change of variables theorem to map the original brick domain into the unit cube as shown in figure 1b.

$$I_\zeta = \hat{\zeta} \cdot \int_0^1 \int_0^1 \int_0^1 \bar{F}(x'(u,v,w), y'(u,v,w), z'(u,v,w))|J(u,v,w)|\, du\, dv\, dw \tag{5}$$

which is accomplished by allowing

$$x'(u,v,w) = \sum_{i=1}^{8} N_i(u,v,w)\, x_i' \tag{6}$$

$$y'(u,v,w) = \sum_{i=1}^{8} N_i(u,v,w)\, y_i' \tag{7}$$

$$z'(u,v,w) = \sum_{i=1}^{8} N_i(u,v,w)\, z_i' \tag{8}$$

with $(x_i', y_i', z_i')$ denoting the $i$th node coordinates as shown in figure 1a. The shape functions are given by

$$
\begin{array}{llll}
N_1(u,v,w) & = & (1-u)(1-v)(1-w) & \quad N_5(u,v,w) & = & (1-u)(1-v)w \\
N_2(u,v,w) & = & u(1-v)(1-w) & \quad N_6(u,v,w) & = & u(1-v)w \\
N_3'u,v,w) & = & uv(1-w) & \quad N_7(u,v,w) & = & uvw \\
N_4(u,v,w) & = & (1-u)v(1-w) & \quad N_8(u,v,w) & = & (1-u)vw
\end{array}
\tag{9}
$$

and the Jacobian is of the form

$$
\begin{aligned}
|J(u,v,w)| = & \frac{\partial x'}{\partial u}\frac{\partial y'}{\partial v}\frac{\partial z'}{\partial w} - \frac{\partial x'}{\partial u}\frac{\partial y'}{\partial w}\frac{\partial z'}{\partial v} - \frac{\partial y'}{\partial u}\frac{\partial x'}{\partial v}\frac{\partial z'}{\partial w} \\
& + \frac{\partial y'}{\partial u}\frac{\partial x'}{\partial w}\frac{\partial z'}{\partial v} + \frac{\partial z'}{\partial u}\frac{\partial x'}{\partial v}\frac{\partial y'}{\partial w} - \frac{\partial z'}{\partial u}\frac{\partial x'}{\partial w}\frac{\partial y'}{\partial v}
\end{aligned}
\tag{10}
$$

2

# 1   Introduction

Edge-based expansion functions have become popular in finite element and moment method techniques applied to the solution of electromagnetic scattering problems. This is due to the fact that the expansion functions are divergenceless within the element domain while any fictitious charges formed at the edges of the element will be canceled by another edge resulting in a volume which is divergenceless. In contrast, nodal expansion functions are not divergenceless and are thus less accurate.

Tanner and Peterson [1] presented triangular and tetrahedral divergence-less vector elements while Jin and Volakis [2] applied the corresponding rectangular brick elements to slot scattering problems. Kameari [3] presented distorted linear and quadratic brick elements in the context of transient quasi-magnetostatic problems.

In this report we derive edge-based expansion functions for a variety of three-dimensional elements. These expansion functions are characterized by unit value along one edge of the element while vanishing along all the remaining edges which are parallel to the unit edge. Distorted bricks, distorted triangular prisms, cylindrical shells and pie-shaped prisms will be presented. The first two of these are suited for completely general inhomogeneous domains whereas the last two are more appropriate for domains terminated at cylindrical boundaries.

# 2   Distorted Brick Element

The first element considered is the distorted brick which is shown in figure 1a. The strategy used herein is to first employ the change of variable theorem to convert the integration domain from the original distorted brick into a cube. Once this is accomplished, the vector-valued function may be expanded in terms of edge-based expansion functions as was done by Jin and Volakis[2]. Typically, one wishes to integrate some vector-valued function

$$\bar{I}(x,y,z) = \int_V \bar{F}(x',y',z',x,y,z)\,dx'\,dy'\,dz' \qquad (1)$$

over the domain of the element where $V$ is the volume of the brick and the vector valued integrand is typically of the form

$$\bar{F}(x',y',z') = \bar{E}(x',y',z')\,G(x',y',z',x,y,z) \qquad (2)$$

1

where $\bar{E}$ is the electric field and $G$ is a Green's function. For the remainder of this report, we suppress the dependence of F on the unprimed coordinates since there will be no operations carried out in these coordinates. Furthermore, we express (1) in terms of its cartesian components

$$\bar{I} = \hat{x}I_x + \hat{y}I_y + \hat{z}I_z \tag{3}$$

where

$$I_\zeta = \hat{\zeta} \cdot \int_V \bar{F}(x',y',z')\,dx'\,dy'\,dz' \tag{4}$$

and $\zeta \in \{\, x,y,z \,\}$.

To evaluate (4), we apply the change of variables theorem to map the original brick domain into the unit cube as shown in figure 1b.

$$I_\zeta = \hat{\zeta} \cdot \int_0^1\!\!\int_0^1\!\!\int_0^1 \bar{F}(x'(u,v,w), y'(u,v,w), z'(u,v,w))|J(u,v,w)|\,du\,dv\,dw \tag{5}$$

which is accomplished by allowing

$$x'(u,v,w) = \sum_{i=1}^{8} N_i(u,v,w)\,x_i' \tag{6}$$

$$y'(u,v,w) = \sum_{i=1}^{8} N_i(u,v,w)\,y_i' \tag{7}$$

$$z'(u,v,w) = \sum_{i=1}^{8} N_i(u,v,w)\,z_i' \tag{8}$$

with $(x_i', y_i', z_i')$ denoting the $i$th node coordinates as shown in figure 1a. The shape functions are given by

$$
\begin{aligned}
N_1(u,v,w) &= (1-u)(1-v)(1-w) & N_5(u,v,w) &= (1-u)(1-v)w \\
N_2(u,v,w) &= u(1-v)(1-w) & N_6(u,v,w) &= u(1-v)w \\
N_3(u,v,w) &= uv(1-w) & N_7(u,v,w) &= uvw \\
N_4(u,v,w) &= (1-u)v(1-w) & N_8(u,v,w) &= (1-u)vw
\end{aligned}
\tag{9}
$$

and the Jacobian is of the form

$$
\begin{aligned}
|J(u,v,w)| \;=\; & \frac{\partial x'}{\partial u}\frac{\partial y'}{\partial v}\frac{\partial z'}{\partial w} - \frac{\partial x'}{\partial u}\frac{\partial y'}{\partial w}\frac{\partial z'}{\partial v} - \frac{\partial y'}{\partial u}\frac{\partial x'}{\partial v}\frac{\partial z'}{\partial w} \\
& + \frac{\partial y'}{\partial u}\frac{\partial x'}{\partial w}\frac{\partial z'}{\partial v} + \frac{\partial z'}{\partial u}\frac{\partial x'}{\partial v}\frac{\partial y'}{\partial w} - \frac{\partial z'}{\partial u}\frac{\partial x'}{\partial w}\frac{\partial y'}{\partial v}
\end{aligned}
\tag{10}
$$

2

The partial derivatives are computed from

$$\frac{\partial \zeta}{\partial \nu} = \sum_{i=1}^{8} \frac{\partial N_i}{\partial \nu}(u, v, w)\zeta_i \qquad (11)$$

with $\zeta \in \{ x, y, z \}$ and $\nu \in \{ u, v, w \}$. From (9) the partial derivatives of the shape functions are found to be

$$\frac{\partial N_1(u, v, w)}{\partial u} = -(1 - v)(1 - w) \qquad \frac{\partial N_5(u, v, w)}{\partial u} = -(1 - v)w$$

$$\frac{\partial N_2(u, v, w)}{\partial u} = (1 - v)(1 - w) \qquad \frac{\partial N_6(u, v, w)}{\partial u} = (1 - v)w$$

$$\frac{\partial N_3(u, v, w)}{\partial u} = v(1 - w) \qquad \frac{\partial N_7(u, v, w)}{\partial u} = vw$$

$$\frac{\partial N_4(u, v, w)}{\partial u} = -v(1 - w) \qquad \frac{\partial N_8(u, v, w)}{\partial u} = -vw$$

$$\frac{\partial N_1(u, v, w)}{\partial v} = -(1 - u)(1 - w) \qquad \frac{\partial N_5(u, v, w)}{\partial v} = -(1 - u)w$$

$$\frac{\partial N_2(u, v, w)}{\partial v} = -u(1 - w) \qquad \frac{\partial N_6(u, v, w)}{\partial v} = -uw$$

$$\frac{\partial N_3(u, v, w)}{\partial v} = u(1 - w) \qquad \frac{\partial N_7(u, v, w)}{\partial v} = uw$$

$$\frac{\partial N_4(u, v, w)}{\partial v} = (1 - u)(1 - w) \qquad \frac{\partial N_8(u, v, w)}{\partial v} = (1 - u)w$$

$$\frac{\partial N_1(u, v, w)}{\partial w} = -(1 - u)(1 - v) \qquad \frac{\partial N_5(u, v, w)}{\partial w} = (1 - u)(1 - v)$$

$$\frac{\partial N_2(u, v, w)}{\partial w} = -u(1 - v) \qquad \frac{\partial N_6(u, v, w)}{\partial w} = u(1 - v)$$

$$\frac{\partial N_3(u, v, w)}{\partial w} = -uv \qquad \frac{\partial N_7(u, v, w)}{\partial w} = uv$$

$$\frac{\partial N_4(u, v, w)}{\partial w} = -(1 - u)v \qquad \frac{\partial N_8(u, v, w)}{\partial w} = (1 - u)v$$

3

Now that we have transformed the integration domain from the original distorted brick into the unit cube, we may expand the vector-valued integral in terms of an edge-based expansion of the form

$$\bar{F}(x'(u,v,w), y'(u,v,w), z'(u,v,w)) = \sum_{j=1}^{12} \bar{N}_j^e(u,v,w)\psi_j \qquad (12)$$

where

$$
\begin{aligned}
\bar{N}_1^e(u,v,w) &= (1-v)(1-w)\hat{t}_{12} & \bar{N}_7^e(u,v,w) &= u(1-w)\hat{t}_{58} \\
\bar{N}_2^e(u,v,w) &= v(1-w)\hat{t}_{43} & \bar{N}_8^e(u,v,w) &= uw\hat{t}_{67} \\
\bar{N}_3^e(u,v,w) &= (1-v)w\hat{t}_{56} & \bar{N}_9^e(u,v,w) &= (1-u)(1-v)\hat{t}_{15} \\
\bar{N}_4^e(u,v,w) &= vw\hat{t}_{87} & \bar{N}_{10}^e(u,v,w) &= u(1-v)\hat{t}_{26} \\
\bar{N}_5^e(u,v,w) &= (1-u)(1-w)\hat{t}_{14} & \bar{N}_{11}^e(u,v,w) &= (1-u)v\hat{t}_{48} \\
\bar{N}_6^e(u,v,w) &= (1-u)w\hat{t}_{23} & \bar{N}_{12}^e(u,v,w) &= uv\hat{t}_{37}
\end{aligned}
$$

$$(13)$$

in which $\psi_j$ are the unknown expansion coefficients and $\hat{t}_{ij}$ denote the element's unit edge vectors given by

$$\hat{t}_{ij} = \frac{\bar{r}_j - \bar{r}_i}{|\bar{r}_j - \bar{r}_i|} \qquad (14)$$

with $\bar{r}_j$ being the position vectors in the original domain.

We may now express the cartesian components of (3) as

$$I_\zeta = \hat{\zeta} \cdot \sum_{j=1}^{12} \psi_j \int_0^1 \int_0^1 \int_0^1 \bar{N}_j^e(u,v,w)|J(u,v,w)|\, du\, dv\, dw \qquad (15)$$

recognizing that $\psi_j$ represents the average component of the vector-valued function associated with the $j$th edge.

It should be noted that the brick cannot be too distorted. This is due to the change of variables theorem. In order to assure a one-to-one mapping for $(x, y, z)$ to $(u, v, w)$, the sign of the Jacobian may not change. This condition will preclude elements that are twisted or extremely narrow and diamond shaped. The typical element should therefore not deviate much from the rectangular brick.

4

# 3  Distorted Triangular Prism

A triangular prism element such as the one shown in figure 2a may be developed in exactly the same manner as the brick. In this case, we employ a mapping from the original volume $V$ to the volume shown in figure 2b followed by an edge-based expansion of the vector-valued integrand. The cartesian component integral may be expressed as

$$I_\zeta = \hat{\zeta} \cdot \int_0^1 \int_0^1 \int_0^{1-u} \bar{F}(x'(u,v,w), y'(u,v,w), z'(u,v,w)) |J(u,v,w)| \, dv \, du \, dw \tag{16}$$

where the coordinate mapping is given by

$$x'(u,v,w) = \sum_{i=1}^{6} N_i(u,v,w) \, x_i' \tag{17}$$

$$y'(u,v,w) = \sum_{i=1}^{6} N_i(u,v,w) \, y_i' \tag{18}$$

$$z'(u,v,w) = \sum_{i=1}^{6} N_i(u,v,w) \, z_i' \tag{19}$$

with the node coordinates $(x_i', y_i', z_i')$ shown in figure 2a and the shape functions are given by

$$
\begin{aligned}
N_1(u,v,w) &= (1-u-v)(1-w) & N_4(u,v,w) &= (1-u-v)w \\
N_2(u,v,w) &= u(1-w) & N_5(u,v,w) &= uw \\
N_3(u,v,w) &= v(1-w) & N_6(u,v,w) &= vw
\end{aligned}
\tag{20}
$$

The Jacobian is again given by (10) with

$$\frac{\partial \zeta}{\partial \nu} = \sum_{i=1}^{6} \frac{\partial N_i}{\partial \nu}(u,v,w)\zeta_i \tag{21}$$

5

and the non-zero shape partial derivatives of $N_i$ are

$$\frac{\partial N_1}{\partial u} = -(1-w) = \frac{\partial N_1}{\partial v} \qquad \frac{\partial N_1}{\partial w} = -(1-u-v) = -\frac{\partial N_4}{\partial w}$$

$$\frac{\partial N_2}{\partial u} = (1-w) = \frac{\partial N_3}{\partial v} \qquad \frac{\partial N_2}{\partial w} = -u = -\frac{\partial N_5}{\partial w}$$

$$\frac{\partial N_4}{\partial u} = -w = \frac{\partial N_4}{\partial v} \qquad \frac{\partial N_3}{\partial w} = -v = -\frac{\partial N_6}{\partial w} \tag{22}$$

$$\frac{\partial N_5}{\partial u} = w = \frac{\partial N_6}{\partial v}$$

The vector valued function in (16) is expanded in terms of edge-based functions

$$\bar{F}(x'(u,v,w), y'(u,v,w), z'(u,v,w)) = \sum_{j=1}^{9} \bar{N}_j^e(u,v,w)\,\psi_j \tag{23}$$

where the vector expansion functions are

$$
\begin{aligned}
\bar{N}_1^e(u,v,w) &= [(\xi_1 + \xi_2)\hat{t}_{12} + \xi_2\hat{t}_{13}](1-w)\\
\bar{N}_2^e(u,v,w) &= -\sqrt{2}[\xi_3\hat{t}_{12} - \xi_2\hat{t}_{13}](1-w)\\
\bar{N}_3^e(u,v,w) &= -[\xi_3\hat{t}_{12} + (\xi_1 + \xi_3)\hat{t}_{13}](1-w)\\
\bar{N}_4^e(u,v,w) &= [(\xi_1 + \xi_2)\hat{t}_{45} + \xi_2\hat{t}_{46}]w\\
\bar{N}_5^e(u,v,w) &= -\sqrt{2}[\xi_3\hat{t}_{45} + \xi_2\hat{t}_{46}]w\\
\bar{N}_6^e(u,v,w) &= -[\xi_3\hat{t}_{45} + (\xi_1 + \xi_3)\hat{t}_{46}]w\\
\bar{N}_7^e(u,v,w) &= u(1-v)\hat{t}_{25}\\
\bar{N}_8^e(u,v,w) &= (1-u)(1-v)\hat{t}_{14}\\
\bar{N}_9^e(u,v,w) &= (1-u)v\hat{t}_{36}
\end{aligned}
\tag{24}
$$

where the area coordinates in (24) are given for the new integration domain

$$
\begin{aligned}
\xi_n &= 2\sqrt{s_n(s_n - a_n)(s_n - b_n)(s_n - c_n)}\\
s_n &= \frac{1}{2}(a_n + b_n + c_n)\\
n &\in \{1,2,3\}
\end{aligned}
\tag{25}
$$

6

and

$$a_1 = \sqrt{(u-1)^2 + v^2} \qquad a_2 = \sqrt{u^2 + (v-1)^2} \qquad a_3 = \sqrt{u^2 + v^2}$$
$$b_1 = \sqrt{u^2 + (v-1)^2} \qquad b_2 = \sqrt{u^2 + v^2} \qquad b_3 = \sqrt{(u-1)^2 + v^2}$$
$$c_1 = \sqrt{2} \qquad c_2 = 1 \qquad c_3 = 1 \tag{26}$$

We are now able to express (16) as

$$I_\zeta = \sum_{j=1}^{9} \psi_j \int_0^1 \int_0^1 \int_0^{1-u} \bar{N}_j^e(u,v,w) |J(u,v,w)| \, dv \, du \, dw \tag{27}$$

realizing that the same limited distortion constraint exists for the triangular prism as was the case for the brick.

# 4  Cylindrical Shell Edge-Based Elements

Although the brick and triangular prism elements given previously are quite general, we find it advantageous to develop an element which is designed for cylindrical problems. The resulting formulation will be quite compact compared to the brick for example since a specific geometry is assumed. This element is the polar cylindrical coordinate equivalent of the brick introduced by Jin and Volakis [2] and is shown in figure 3.

For cylindrical problems, we wish to evaluate the integral

$$\bar{I} = \int_{z_1}^{z_5} \int_{\phi_1}^{\phi_2} \int_{\rho_1}^{\rho_4} \bar{F}(\rho', \phi', z') \rho' \, d\rho' \, d\phi' \, dz' \tag{28}$$

where the vector-valued function $\bar{F}(\rho', \phi', z')$ is analogous to (2). We do not employ any change of variable for this element so we may directly express the vector-valued function in terms of an edge-based expansion

$$\bar{F}(\rho', \phi', z') = \sum_{j=1}^{12} \bar{N}_j^e(\rho', \phi', z') \, \psi_j \tag{29}$$

The shape functions are given by

$$\bar{N}_1^e(\rho', \phi', z') = \left[\frac{\rho_4^2 - \rho'^2}{\rho_4^2 - \rho_1^2}\right] \left[\frac{z' - z_5}{z_1 - z_5}\right] \hat{\phi}$$

7

$$\bar{N}_2^e(\rho', \phi', z') = \left[1 - \frac{|\phi_2 - \phi'|}{|\phi_2 - \phi_1|}\right]\left[\frac{z' - z_5}{z_1 - z_5}\right]\hat{\rho}$$

$$\bar{N}_3^e(\rho', \phi', z') = \left[\frac{\rho'^2 - \rho_1^2}{\rho_4^2 - \rho_1^2}\right]\left[\frac{z' - z_5}{z_1 - z_5}\right]\hat{\phi}$$

$$\bar{N}_4^e(\rho', \phi', z') = \left[1 - \frac{|\phi' - \phi_1|}{|\phi_2 - \phi_1|}\right]\left[\frac{z' - z_5}{z_1 - z_5}\right]\hat{\rho}$$

$$\bar{N}_5^e(\rho', \phi', z') = \left[\frac{\rho_4^2 - \rho'^2}{\rho_4^2 - \rho_1^2}\right]\left[\frac{z' - z_1}{z_1 - z_5}\right]\hat{\phi}$$

$$\bar{N}_6^e(\rho', \phi', z') = \left[1 - \frac{|\phi_2 - \phi'|}{|\phi_2 - \phi_1|}\right]\left[\frac{z' - z_1}{z_5 - z_1}\right]\hat{\rho}$$

$$\bar{N}_7^e(\rho', \phi', z') = \left[\frac{\rho'^2 - \rho_1^2}{\rho_4^2 - \rho_1^2}\right]\left[\frac{z' - z_1}{z_5 - z_1}\right]\hat{\phi}$$

$$\bar{N}_8^e(\rho', \phi', z') = \left[1 - \frac{|\phi' - \phi_1|}{|\phi_2 - \phi_1|}\right]\left[\frac{z' - z_1}{z_5 - z_1}\right]\hat{\rho}$$

$$\bar{N}_9^e(\rho', \phi', z') = \left[\frac{\rho_4 - \rho'}{\rho_4 - \rho_1}\right]\left[\frac{|\phi_2 - \phi'|}{|\phi_2 - \phi_1|}\right]\hat{z}$$

$$\bar{N}_{10}^e(\rho', \phi', z') = \left[\frac{\rho_4 - \rho'}{\rho_4 - \rho_1}\right]\left[\frac{|\phi' - \phi_1|}{|\phi_2 - \phi_1|}\right]\hat{z}$$

$$\bar{N}_{11}^e(\rho', \phi', z') = \left[\frac{\rho' - \rho_1}{\rho_4 - \rho_1}\right]\left[\frac{|\phi' - \phi_1|}{|\phi_2 - \phi_1|}\right]\hat{z}$$

$$\bar{N}_{12}^e(\rho', \phi', z') = \left[\frac{\rho' - \rho_1}{\rho_4 - \rho_1}\right]\left[\frac{|\phi_2 - \phi'|}{|\phi_2 - \phi_1|}\right]\hat{z} \qquad (30)$$

where $(\rho_i, \phi_i, z_i)$ denote the node coordinates as shown in figure 3 and (28) is given by

$$\bar{I} = \sum_{j=1}^{12} \psi_j \int_{z_1}^{z_5}\int_{\phi_1}^{\phi_2}\int_{\rho_1}^{\rho_4} \bar{N}_j^e(\rho', \phi', z') \, \rho' \, d\rho' \, d\phi' \, dz' \qquad (31)$$

8

# 5 Pie-Shaped Prism

The final element considered is the complement to the cylindrical shell element, the pie-shaped element which is shown in figure 4. The development of this element closely parallels the previous element.

The vector-valued integral is given by

$$\bar{I} = \int_{z_1}^{z_5} \int_{\phi_2}^{\phi_3} \int_{\rho_1}^{\rho_2} \bar{F}(\rho', \phi', z') \, \rho' \, d\rho' \, d\phi' \, dz' \tag{32}$$

The vector-valued function is expanded in terms of edge vectors

$$\bar{F}(\rho', \phi', z') = \sum_{j=1}^{9} \bar{N}_j^e(\rho', \phi', z') \, \psi_j \tag{33}$$

and the edge-based expansion functions are

$$
\begin{aligned}
\bar{N}_1^e(\rho', \phi', z') &= \left[1 - \frac{|\phi' - \phi_2|}{|\phi_3 - \phi_2|}\right] \left[\frac{z_4 - z'}{z_4 - z_1}\right] \hat{\rho} \\
\bar{N}_2^e(\rho', \phi', z') &= \left[\frac{\rho' - \rho_1}{\rho_4 - \rho_1}\right] \left[\frac{z_4 - z'}{z_4 - z_1}\right] \hat{\phi} \\
\bar{N}_3^e(\rho', \phi', z') &= \left[1 - \frac{|\phi_3 - \phi'|}{|\phi_3 - \phi_2|}\right] \left[\frac{z_4 - z'}{z_4 - z_1}\right] \hat{\rho} \\
\bar{N}_4^e(\rho', \phi', z') &= \left[1 - \frac{|\phi' - \phi_2|}{|\phi_3 - \phi_2|}\right] \left[\frac{z' - z_1}{z_4 - z_1}\right] \hat{\rho} \\
\bar{N}_5^e(\rho', \phi', z') &= \left[\frac{\rho' - \rho_1}{\rho_2 - \rho_1}\right] \left[\frac{z' - z_1}{z_4 - z_1}\right] \hat{\phi} \\
\bar{N}_6^e(\rho', \phi', z') &= \left[1 - \frac{|\phi_3 - \phi'|}{|\phi_3 - \phi_2|}\right] \left[\frac{z' - z_1}{z_4 - z_1}\right] \hat{\rho} \\
\bar{N}_7^e(\rho', \phi', z') &= \left[\frac{\rho' - \rho_1}{\rho_2 - \rho_1}\right] \left[\frac{|\phi_3 - \phi'|}{|\phi_3 - \phi_2|}\right] \hat{z} \\
\bar{N}_8^e(\rho', \phi', z') &= \left[\frac{\rho' - \rho_1}{\rho_2 - \rho_1}\right] \left[\frac{|\phi' - \phi_2|}{|\phi_3 - \phi_2|}\right] \hat{z} \\
\bar{N}_9^e(\rho', \phi', z') &= \left[\frac{\rho_2 - \rho'}{\rho_2 - \rho_1}\right] \hat{z}
\end{aligned} \tag{34}
$$

where $(\rho_i, \phi_i, z_i)$ are the nodal coordinates shown in figure 4. With this expansion, (32) may be written

$$\bar{I} = \sum_{j=1}^{9} \psi_j \int_{z_1}^{z_5} \int_{\phi_2}^{\phi_3} \int_{\rho_1}^{\rho_2} \bar{N}_j^e(\rho', \phi', z')\, \rho'\, d\rho'\, d\phi'\, dz' \qquad (35)$$

# 6  Conclusions

Four different linear volume elements were presented: distorted brick, distorted triangular prism, cylindrical shell, and pie-shaped prism. All of these elements are used to evaluate a vector-valued integral over the volume of the element by employing edge-based vector expansion functions. These functions were explicitly given for all elements. In addition, the shape functions and Jacobian associated with the mapping of the arbitrary brick or triangular prism to a known prism are presented. Since these elements are divergence-less, we expect them to useful for simulating various geometries via the finite element method or the Method of Moments.

# References

[1] David R. Tanner and Andrew F. Peterson, "Vector Expansion Functions for the Numerical Solution of Maxwell's Equations," *Microwave and Optical Tech. Letters*, Sept. 1989.

[2] Jian-Ming Jin and John L. Volakis, "Electromagnetic Scattering by and Transmission Through a Three-Dimensional Slot in a Thick Conducting Plane," *IEEE Trans. Antennas Propagat.*, Vol. 39, No. 4, Apr. 1991.

[3] Akihisa Kameari, "Calculation of Transient 3D Eddy Current using Edge-Elements," *IEEE Trans. Magnetics*, Vol. 26, No. 2, Mar. 1990.
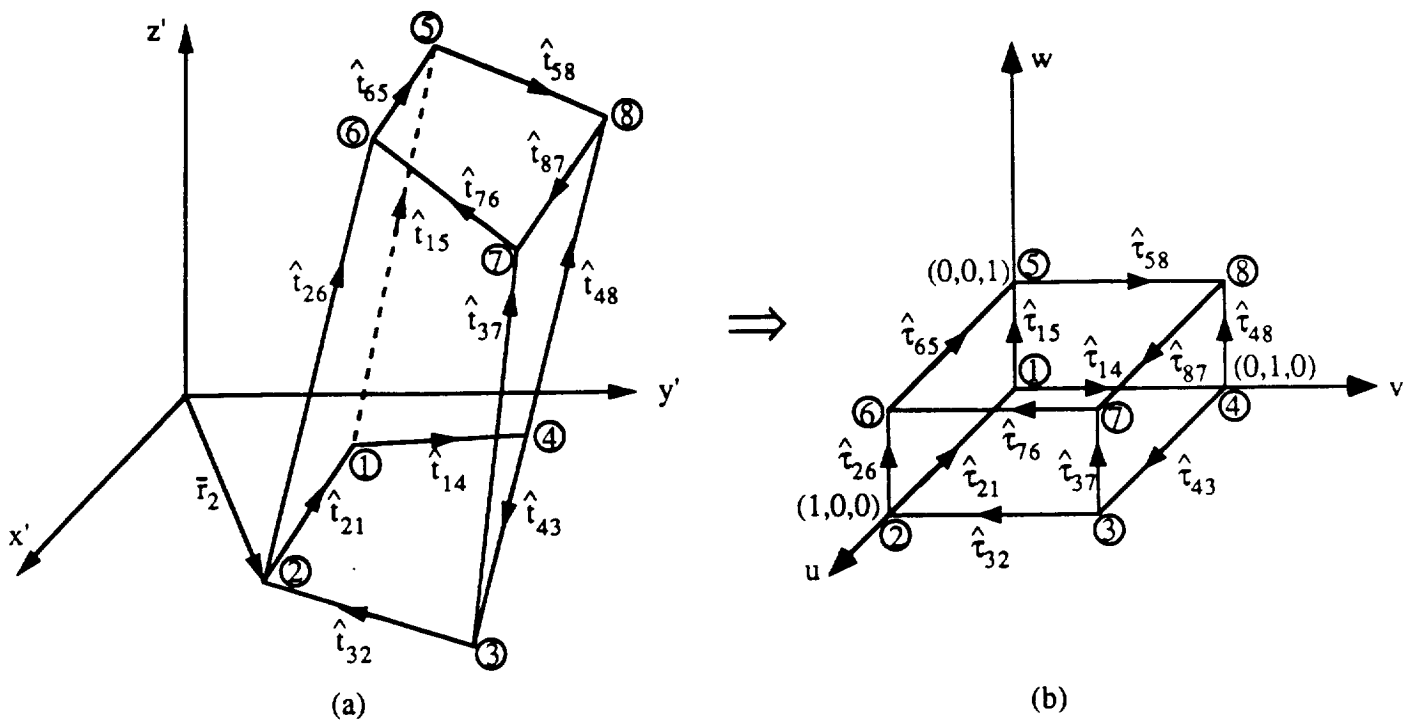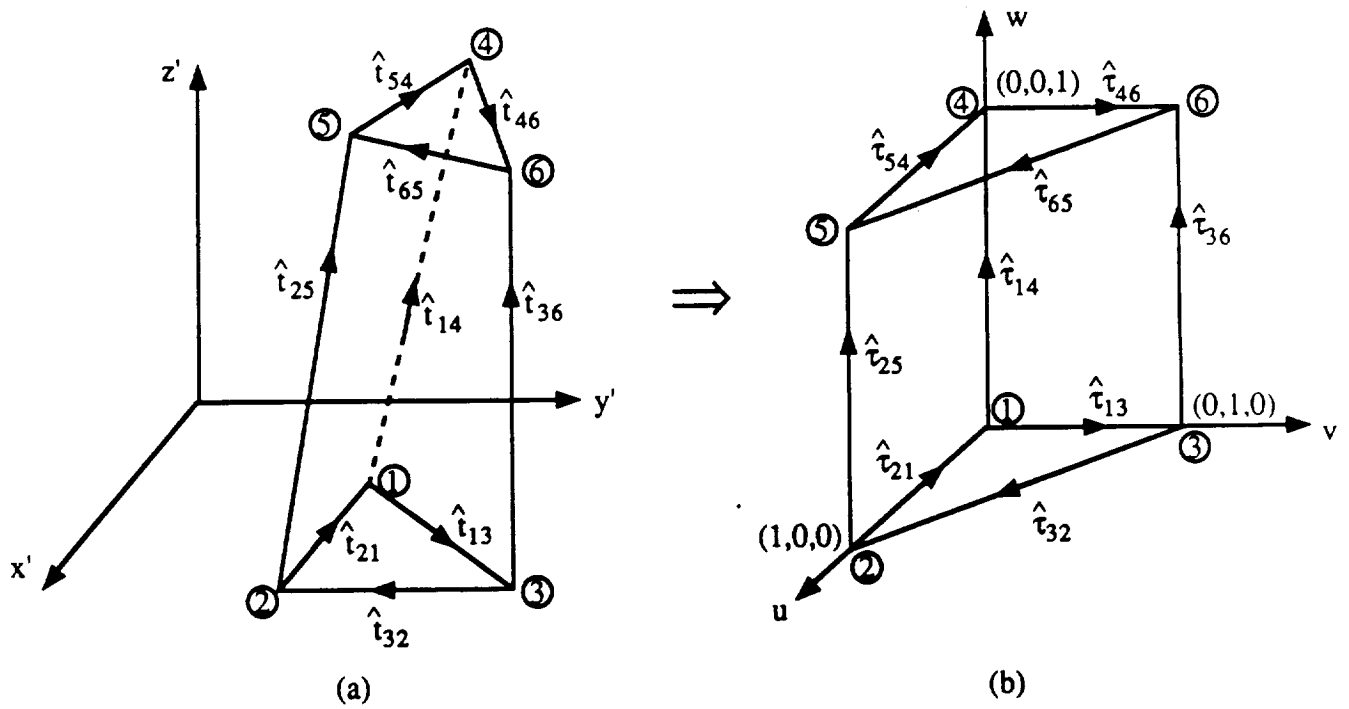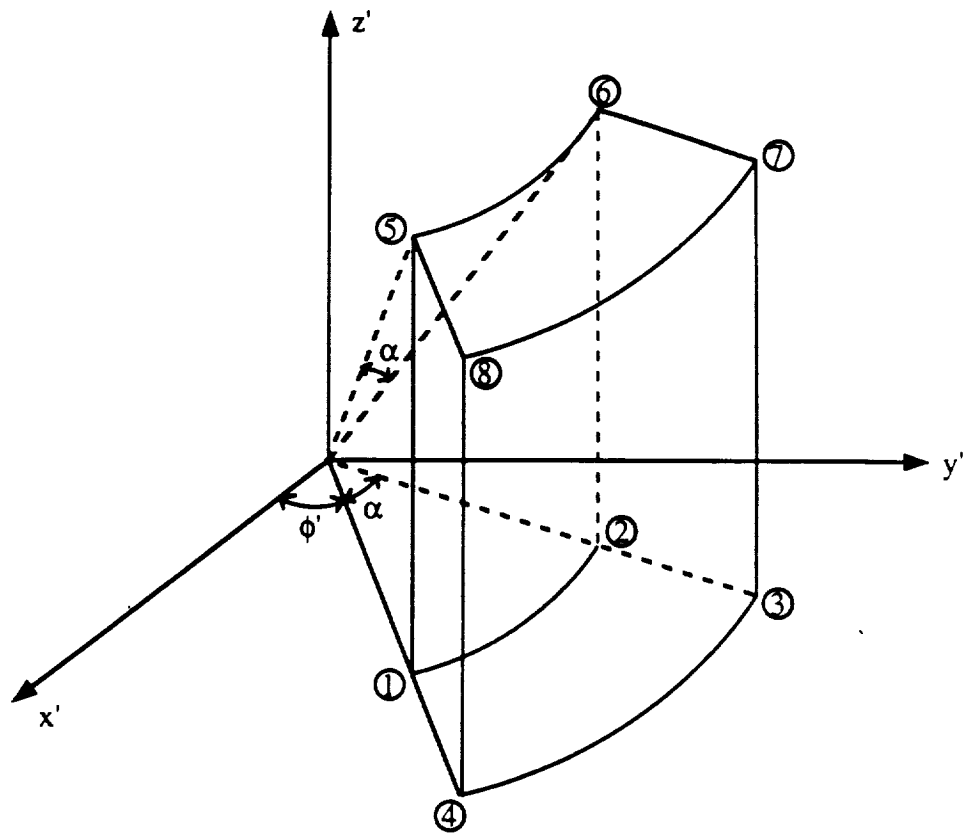
(a)

(b)

Figure 1



(a)

(b)

Figure 2

Figure 3
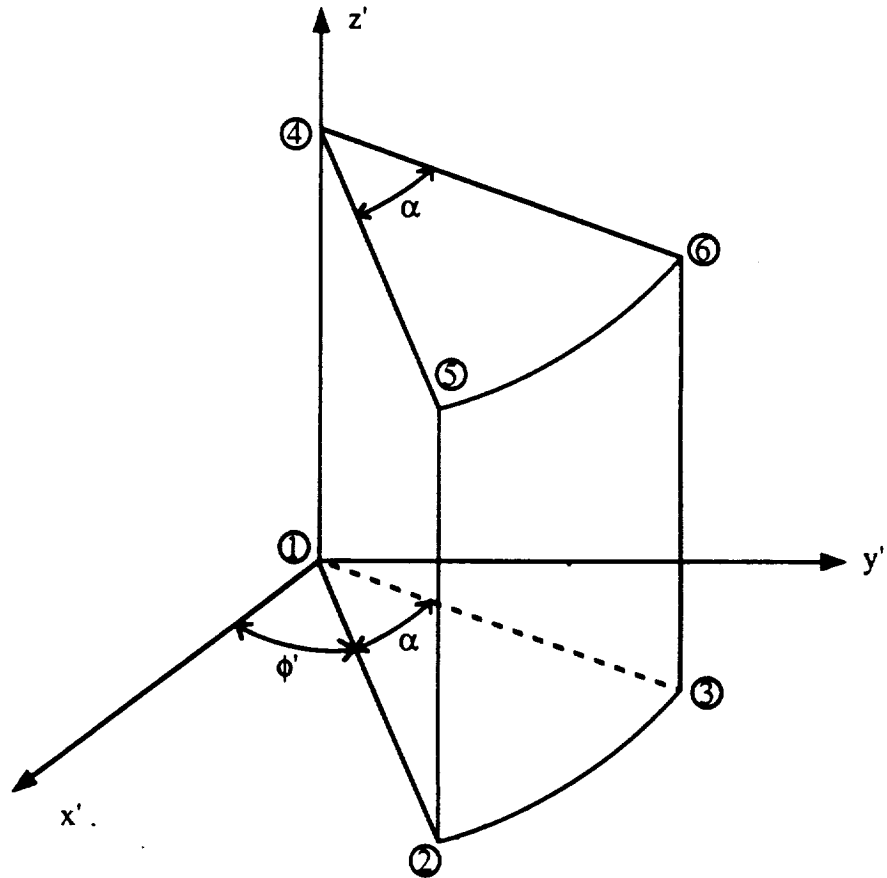


Figure 4

# Modeling of Resistive Sheets in Finite Element Solutions

J.M. Jin, J.L. Volakis
Radiation Laboratory
Department of Electrical Engineering and Computer Science
University of Michigan
Ann Arbor, MI 48109-2122

C.L. Yu
Pacific Missile Test Center
Pt. Mugu, CA 93042-5000
and
A.C. Woo
NASA-Ames Research Center
Moffett Field, CA 94035-1000

**Abstract**

A formulation is presented for modeling a resistive card in the context of the finite element method. The appropriate variational function is derived and for validation purposes results are presented for the scattering by a metal-backed cavity loaded with a resistive card.

1
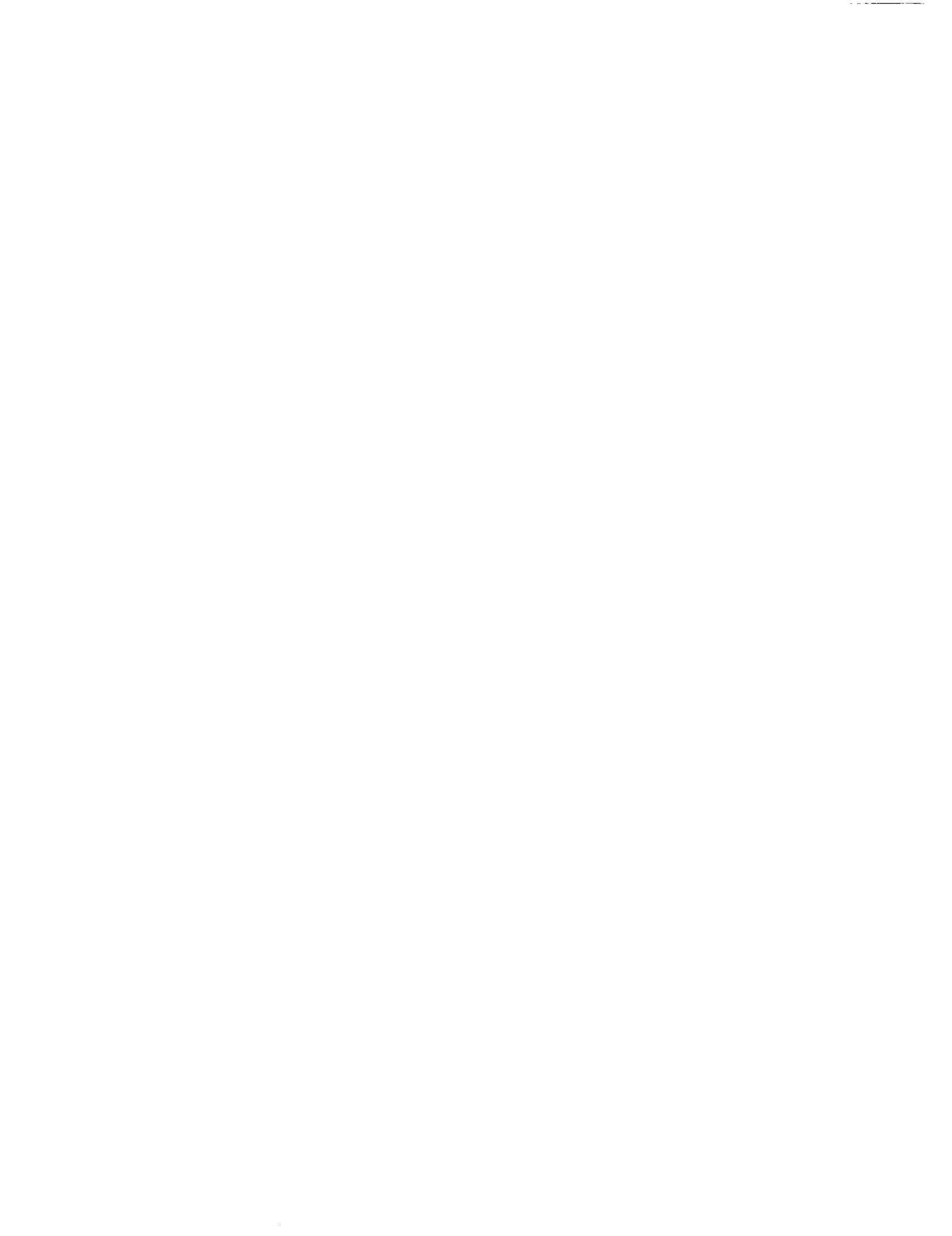
# 1 Introduction

A resistive card is an infinitesimally thin sheet of material which allows partial penetration of the electromagnetic field. Thin dielectric layers and very thin conductors whose thickness is less than the skin depth are examples of materials which can be modelled by resistive cards or sheets. Resistive cards are often used for radar cross section and RF power penetration control and as a result they have been studied extensively. Such studies have generally been done in the context of high frequency [1,2] and integral equation solutions [3,4], but to date the treatment of resistive cards within the context of the finite element method (FEM) has not been considered. Over the past few years, FEM has been applied to a variety of electromagnetic applications and it is thus important to incorporate the modeling of resistive cards in the FEM. In this paper we propose an FEM formulation which accounts for the presence of resistive sheets. To validate this formulation, results based on a physical modeling of the resistive sheet are also presented. In this case, the resistive sheet is equivalently replaced by a thin dielectric layer. The modeling of such a layer in the usual manner leads to larger and consequently inefficient linear systems, which is the primary reason for resorting to a mathematical modeling of the resistive sheet. Results based on the mathematical and physical modeling are presented in connection with the scattering by a metal-backed cavity in a ground plane and these are used to validate the proposed mathematical model.

# 2 Formulation

A resistive sheet is characterized by its resistivity $R$ which is measured in Ohms per square. Mathematically, it satisfies the boundary condition [5

$$\hat{n} \times (\hat{n} \times \mathbf{E}) = -R\hat{n} \times \left( \mathbf{H}^+ - \mathbf{H}^- \right) \tag{1}$$

where $\mathbf{H}^\pm$ denotes the magnetic field above and below the sheet, $\mathbf{E}$ is the electric field and its tangential component is continuous across the sheet, and $\hat{n}$ denotes the unit normal to the sheet pointing in the upward direction (+ side). To a first order, this boundary condition can be used to simulate the

presence of a thin dielectric layer by setting [4,5]

$$R = \frac{Z_o}{j k_o (\epsilon_r - 1) t}$$

In this, $t$ is the thickness of the layer, $Z_o$ and $k_o$ denote the free space intrinsic impedance and wave number, respectively, and $\epsilon_r$ is the relative dielectric constant of the layer. Alternatively, a resistive sheet may be equivalently replaced by a thin dielectric layer having thickness $t$ and a relative permittivity of

$$\epsilon_r = 1 - \frac{j Z_o}{k_o t R} \tag{2}$$

Generally, the accuracy of this simulation increases as the thickness $t$ is decreased. Typically, $t$ should not exceed one-tenth of the wavelength in the material.

Let us now consider a finite element solution of the fields within a volume V subject to a given excitation. The volume consists of some inhomogeneous dielectric having relative permittivity and permeability $\epsilon_r$ and $\mu_r$, respectively, and we shall also assume that resistive cards may be embedded within the dielectric (see Figure 1). In accordance with the finite element method, the volume is subdivided into $M$ smaller volume elements and in this case we require that the resistive cards are tangential to the boundary surface of these elements. A weak solution of the fields within the volume can be obtained by extremizing the functional

$$F = \sum_{e=1}^{M} F^e, \tag{3}$$

$$F^e = \int \int \int_{V_e} \left[ \frac{1}{\mu_r} (\nabla \times \mathbf{E}) \cdot (\nabla \times \mathbf{E}) - k_o^2 \epsilon_r \mathbf{E} \cdot \mathbf{E} \right] dv$$

$$+ j k_o Z_o \oiint_{S_e} \mathbf{E} \cdot (\mathbf{H} \times \hat{n}_e) \, ds \tag{4}$$

with respect to the electric field $\mathbf{E}$ including that implied in $\mathbf{H}$. In this expression, $V_e$ is the volume of the element which is enclosed by the surface $S_e$ and $\hat{n}_e$ denotes the outward normal to $S_e$.

3

Generally, for a dielectric volume not enclosing resistive sheets or other current sheets, the contributions of the surface integrals in (3)-(4) vanish everywhere except when $S_e$ coincides with the outer surface $S_o$ of the volume V. This is a consequence of field continuity across the elements, but if a portion of the element's surface coincides with a resistive sheet, then the surface integral in (4) does not vanish since the magnetic field is discontinuous as described in (1). Let us for example consider the surface $S_{re}$ which borders the $e$th and $(e + 1)$th elements, and is coincident with a resistive sheet of resistivity $R$. Then the contribution from this surface to the surface integral in (4) is

$$j k_o Z_o \int \int_{S_{re}} \mathbf{E} \cdot \left( \mathbf{H}^- \times \hat{n}_{re} \right) ds$$

from the $e$th element and

$$-j k_o Z_o \int \int_{S_{re}} \mathbf{E} \cdot \left( \mathbf{H}^+ \times \hat{n}_{re} \right) ds$$

from the $(e + 1)$th element with $\hat{n}_{re}$ pointing from the $e$th to the $(e + 1)$th element. Combining these two integrals and employing (1), it follows that the contribution of the surface $S_{re}$ to the surface integral in (4) is

$$- j k_o Z_o \int \int_{S_{re}} \left[ \mathbf{E} \cdot \left( \mathbf{H}^+ - \mathbf{H}^- \right) \times \hat{n}_{re} \right] ds$$

$$= j k_o Z_o \int \int_{S_{re}} \frac{1}{R} \left( \hat{n}_{re} \times \mathbf{E} \right) \cdot \left( \hat{n}_{re} \times \mathbf{E} \right) ds \qquad (5)$$

Consequently, the functional $F$ may be rewritten as

$$F = \sum_{e=1}^{M} \int \int \int_{V_e} \left\{ \frac{1}{\mu_r} (\nabla \times \mathbf{E}) \cdot (\nabla \times \mathbf{E}) - k_o^2 \epsilon_r \mathbf{E} \cdot \mathbf{E} \right\} dv$$

$$+ j k_o Z_o \int \int_{S_r} \frac{1}{R} \left( \hat{n}_r \times \mathbf{E} \right) \cdot \left( \hat{n}_r \times \mathbf{E} \right) ds$$

$$+ j k_o Z_o \oiint_{S_o} \mathbf{E} \cdot \left( \mathbf{H} \times \hat{n}_o \right) ds \qquad (6)$$

in which $S_r$ denotes the surface occupied by the resistive sheet and $S_o$ is the outer surface enclosing the volume V. As usual, $\hat{n}_r$ is the outward normal to $S_r$ and $\hat{n}_o$ is correspondingly the outward normal to $S_o$. If $S_r$ borders the

outer surface of the volume V, then $S_o$ should be considered to be just over the exterior side of $S_r$ (i.e., $S_o$ always encloses $S_r$).

Having derived the explicit form of the functional $F$, we may now expand the element field using the standard linear shape functions. If the sources are within V then $F$ should be modified to read

$$
F = \int\int\int_V \left\{ \frac{1}{\mu_r}(\nabla \times \mathbf{E}) \cdot (\nabla \times \mathbf{E}) - k_o^2 \epsilon_r \mathbf{E} \cdot \mathbf{E} \right\} dv
$$

$$
+ \int\int\int_V \mathbf{E} \cdot \left[ j k_o Z_o \mathbf{J}^{int} - \nabla \times \left( \frac{1}{\mu_r} \mathbf{M}^{int} \right) \right] dv
$$

$$
+ j k_o Z_o \int\int_{S_r} \frac{1}{R}(\hat{n}_r \times \mathbf{E}) \cdot (\hat{n}_r \times \mathbf{E}) ds
$$

$$
+ j k_o Z_o \oiint_{S_o} \mathbf{E} \cdot (\mathbf{H} \times \hat{n}_o) ds \qquad (7)
$$

where $(\mathbf{J}^{int}, \mathbf{M}^{int})$ denote the impressed sources internal to V. Then, upon setting the first order variation of $F$ to zero, we can obtain a system of equations for the solution of the interior and boundary electric fields. For a unique solution of this system we must, however, specify a relation between the tangential electric and magnetic field which appear in the surface integral over $S_o$. If we assume that the subject volume is that occupied by the metal-backed cavity recessed in a ground plane, as shown in figure 2, then $S_o$ reduces to the aperture area of that cavity. By invoking image theory, the magnetic field on the aperture can then be expressed as

$$
\mathbf{H} = \mathbf{H}^{inc} + \mathbf{H}^{ref} - 2 j k_o Y_o \int\int_{S_a} \left[ \left( \bar{\mathbf{I}} + \frac{1}{k_o^2} \nabla\nabla \right) G_o(\mathbf{r}, \mathbf{r}') \right] \cdot [\mathbf{E}(\mathbf{r}) \times \hat{z}] ds' \quad (8)
$$

where $S_a$ denotes the aperture surface, $G_o(\mathbf{r}, \mathbf{r}')$ is the free space scalar Green's function, $\mathbf{r}$ specifies the observation point located on $S_a$ and $\bar{\mathbf{I}} = \hat{x}\hat{x} + \hat{y}\hat{y} + \hat{z}\hat{z}$ is the unit dyad. Also, $\mathbf{H}^{inc}$ denotes the magnetic field generated by sources in the free space and $\mathbf{H}^{ref}$ is the corresponding reflected field when the cavity's aperture is shorted. Substituting (8) into (7) gives a functional only in terms of the electric field. The system obtained from this functional will be partly sparse and partly full. In particular the volume

5

integrals and that over $S_r$ in (7) lead to a sparse submatrix involving the interior fields of the cavity. However, in view of (8) the last surface integral of (7) over $S_o$ (or $S_a$) renders a full Toeplitz submatrix since the boundary integral is convolutional. Consequently, by resorting to an iterative solution such as the conjugate or biconjugate gradient method in conjunction with the fast Fourier transform, the need to generate the Toeplitz matrix is eliminated thus maintaining the O(n) storage requirement, characteristic of finite element solutions. The details pertaining to this implementation are discussed in [6] - [8]. In the next section we only present some results aimed at evaluating the accuracy of the proposed resistive sheet model.

## 3 Numerical Results

Let us consider the metal-backed rectangular cavity illustrated in Figure 2. The cavity is assumed to be empty (no internal sources) and is illuminated by a plane wave in the $\phi = 0$ plane. For implementing the aforementioned solution, the cavity is subdivided into rectangular bricks and the results of the solution are shown in Figure 3. These are radar cross section (RCS) patterns and refer to a $1\lambda$ deep cavity whose aperture is also $1\lambda \times 1\lambda$. The RCS pattern in Figure 3(b) applies to the cavity which is loaded with a resistive sheet of $100\Omega/\square$ placed at its aperture, whereas the result in Figure 3(a) is for the untreated empty cavity. The simulation of the resistive sheet was done through direct discretization of the first order variation of the functional $F$ as given in (7) and alternatively by modeling the resistive sheet as a dielectric layer of thickness $\lambda/20$ having the dielectric constant computed from (2). As shown in Figure 3(b) the results based on the two simulations are in reasonable agreement and the differences among them is due to the finite thickness which was necessarily introduced in the physical model of the resistive sheet. As noted in [9] and [10], the dielectric layer introduces vertical components of the electric field which are not present in the resistive sheet. It is certainly of interest to point out that the presence of the resistive sheet at the aperture surface reduced the RCS of the cavity by 10dB at normal incidence and by as much as 20dB at grazing incidence.

The second geometry which was considered is a circular metal-backed cavity again situated in a ground plane. In this case the aperture of the

circular cavity is loaded with a sheet having non-uniform resistivity given by

$$R(\rho) = \begin{cases} Z_o \left[ 0.1 + 10 \left( \frac{a-\rho}{a} \right)^2 \right] & \rho > 0.5a \\ \\ \infty & \text{elsewhere on } S_a \end{cases} \tag{9}$$

where $a$ denotes the radius of the aperture. Results with and without resistive loading for a cavity having $a = 1$in. and a depth of 0.25in. are shown in Figure 4. These RCS patterns were computed at 16GHz and the incident field was a plane wave polarized along the $\theta$ or $\phi$ directions. Again, the data in Figure 4 demonstrate the validity of the proposed mathematical model. Also, as in the case of the rectangular cavity the presence of the resistive cards reduces the overall RCS of the cavity and this reduction is primarily due to the re'u⌣ed field intensity near its perimeter.

# 4    Conclusions

A formulation was derived for modeling resistive cards within the context of the finite element method. Essentially, the pertinent variational functional was supplemented with an additional boundary integral over the surface of the resistive sheet/card. Results based on the discretization of the functional were also presented and these were aimed at demonstrating the accuracy of the derived mathematical model.

# References

[1] T.B.A. Senior, "Scattering by Resistive Strips," *Radio Science*, Vol. **14**, pp. 911-924, 1979.

[2] M.I. Herman and J.L. Volakis, "High Frequency Scattering by a Resistive Strip and Extensions to Conductive and Impedance Strips," *Radio Science*, Vol. **22**, pp. 335-349, May-June 1987.

[3] E.F. Knott and T.B.A. Senior, "Non-Specular Radar Cross Section Study," 'niversity of Michigan Radiation Laboratory Technical Report 011764-ₐ ⌐ (also U.S. Air Force Avionics Lab. report AFAL-TR-73-422) January 1974.

[4] R.F. Harrington and J.R. Mautz, "An Impedance Sheet Approximation for Thin Dielectric Shells," *IEEE Trans. Antennas Propagat.*, Vol. **AP-23**, pp. 531-534, 1975.

[5] T.B.A. Senior, "Combined Resistive and Conductive Sheets," *IEEE Trans. Antennas Propagat.*, Vol. **AP-33**, pp. 577-579, 1985.

[6] J.M. Jin and J.L. Volakis, "A Finite Element-Boundary Integral Formulation for Scattering by Three-Dimensional Cavity-Backed Apertures," *IEEE Trans. Antennas Propagat.*, Vol. **AP-39**, pp. 97-104, January 1991.

[7] J.M. Jin and J.L. Volakis, "Electromagnetic Scattering by and Transmission Through a Three-Dimensional Slot in a Thick Conducting Plane," *IEEE Trans. Antennas Propagat.*, Vol. **AP-39**, pp. 543-550, April 1991.

[8] J.M. Jin and J.L. Volakis, "Scattering and Radiation From Microstrip Patch Antennas and Arrays Residing in a Cavity," submitted to *IEEE Trans. Antennas Propagat.*.

[9] T.B.A. Senior and J.L. Volakis, "Sheet Simulation of Dielectric Layers," *Radio Science*, **22**, Dec. 1987, pp. 1261-1272.

[10] J.L. Volakis, "Numerical Implementation of Generalized Impedance Boundary Conditions," 1989 URSI Electromagnetic Theory Symposium, Aug. 1989, Stockholm, Sweden. Symposium Digest pp. 434-437.

FIGURE CAPTIONS

Fig. 1  Cross Section of a dielectric volume enclosing a resistive card (a) card within the
dielectric  (b) card on the surface of the dielectric

Fig. 2  Geometry of a cavity-backed aperture in a ground plane.

Fig. 3  Monostatic RCS for a rectangular aperture ($1\lambda$ x $1\lambda$) backed by a rectangular cavity
($1\lambda$ x $1\lambda$ x $1\lambda$) in the $\phi=0$ plane.  (a) Empty cavity without resistive loading (b)
Empty cavity whose aperture is covered with a resistive sheet having a resistivity of
$100\Omega/\square$. (Solid and dashed lines correspond to results based on the mathematical
simulation; circles and squares refer to results based on the physical modeling of
the resistive sheet)

Fig. 4  Monostatic RCS for a circular aperture (1 inch in diameter) backed by a circular
cavity (1 inch in diameter and 0.25 inches deep) at 16 GHz.  (a) Empty cavity.  (b)
Empty cavity covered with a resistive sheet whose resistivity is given by equ. (a).
(Solid and dashed lines correspond to results based on the mathematical
simulation; circles and squares refer to results based on the physical modeling of
the resistive sheet)
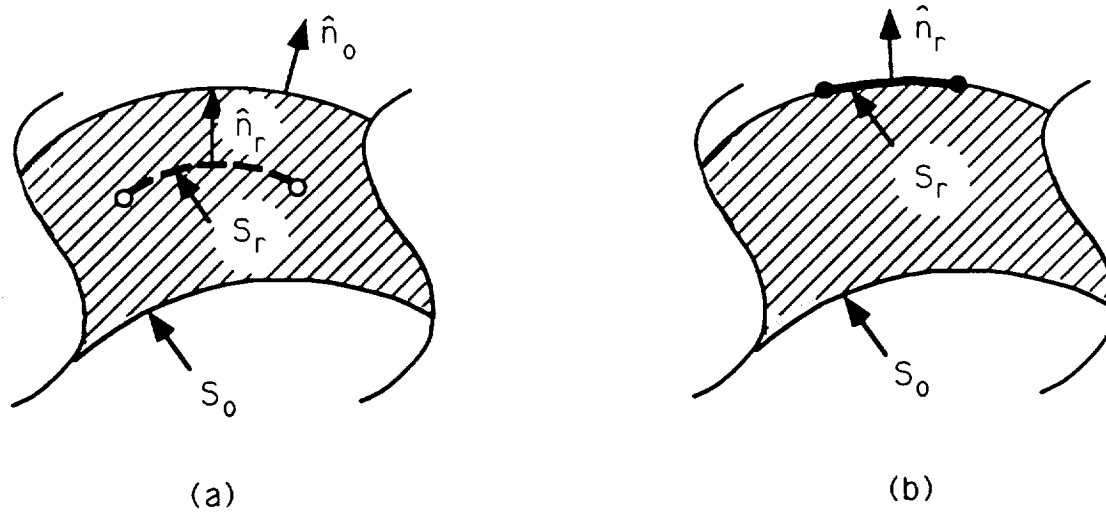
Figure 1.   Cross section of a dielectric volume enclosing a
resistive card  (a) card within the dielectric
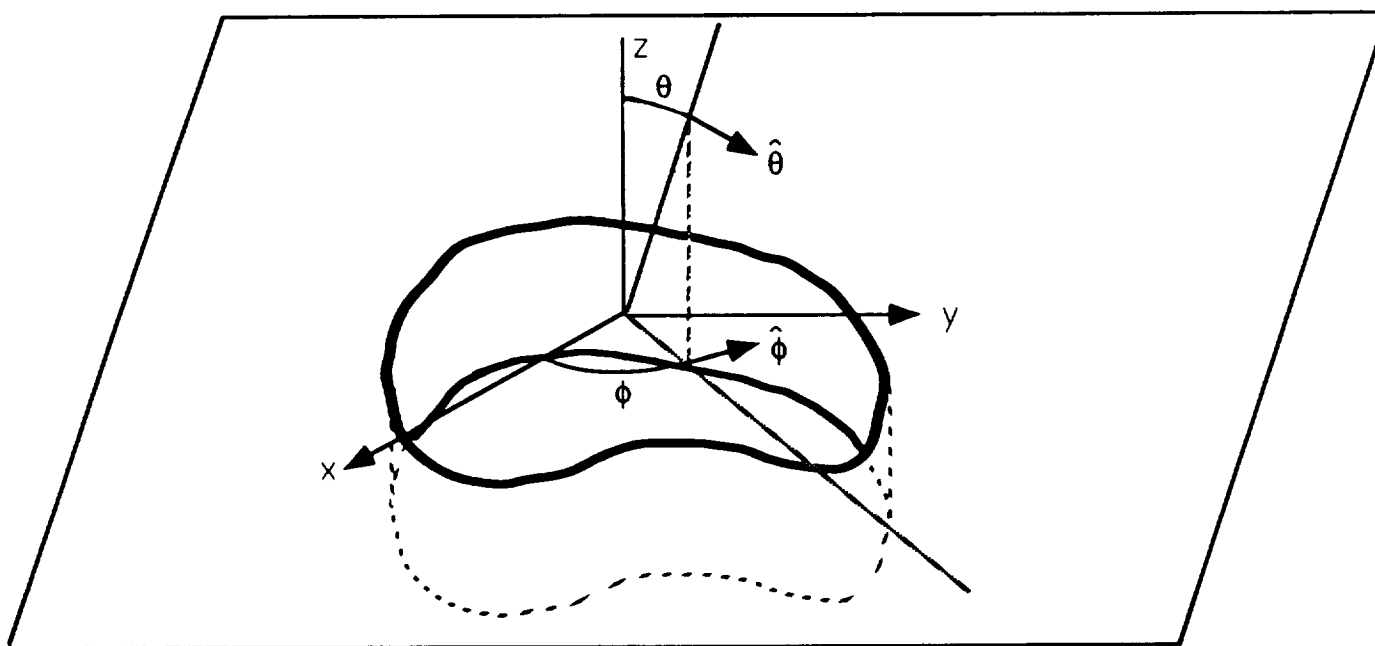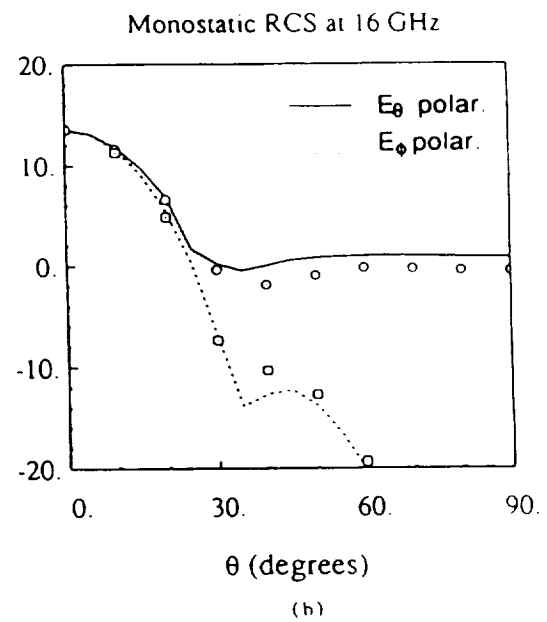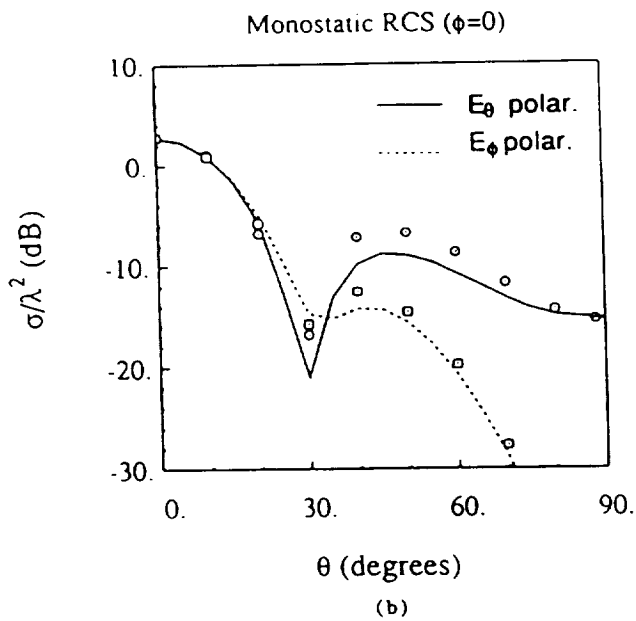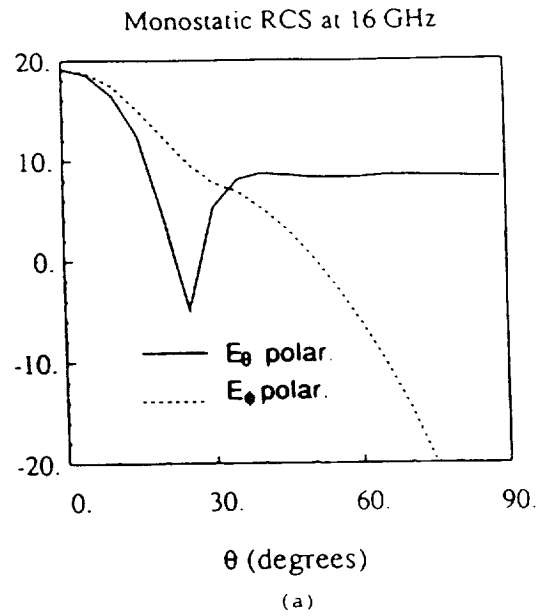(b)  card on the surface of the dielectric



Figure 2

Monostatic RCS (φ=0)

Monostatic RCS at 16 GHz

Monostatic RCS (φ=0)

Monostatic RCS at 16 GHz

(a)

(a)

(b)

(h)

Figure 3

Figure 4